Queensland University of Technology

PhD Thesis by Published Papers

Faster Monte Carlo Simulation of Radiotherapy Geometries

Candidate & Author:
Mr. Christopher Mark Poole

Supervisors:
Prof. Christian Langton
Dr. Jamie Trapp

Submitted to the School of Chemistry, Physics and Mechanical Engineering, Science and Engineering Faculty, Queensland University of Technology, in partial fulfilment of the requirements of the degree of Doctor of Philosophy.

September, 2012

© Copyright Christopher Mark Poole 2012.
All Rights Reserved.

Statement of Authorship

The work contained in this thesis has not been previously submitted for a degree or diploma at any other tertiary educational institution. To the best of my knowledge and belief, this thesis contains no material previously published or written by another person except where due reference is made.

Signature:

Christopher Mark Poole _____ September, 2012

Reproducible Research

> An article about computational science in a scientific publication is not the scholarship itself, it is merely advertising of the scholarship. The actual scholarship is the complete software development environment and the complete set of instructions which generated the figures.
>
> –D. Donoho

In the spirit of reproducible research, the software (including sourcecode, documentation and examples) that has been developed as a part of this thesis has been made freely available online, and can be downloaded from:

http://code.google.com/p/cadmesh/

http://code.google.com/p/manysim/

http://github.com/christopherpoole/

Keywords

CAD, DICOM, DICOM-RT, dosimetry, GEANT4, gel dosimetry, Monte Carlo, cloud computing, compute aided design, organic plastic scintillator, parallel computing, patient geometry, radiation transport, radiotherapy, treatment planning

Abstract

Using Monte Carlo simulation for radiotherapy dose calculation can provide more accurate results when compared to the analytical methods usually found in modern treatment planning systems, especially in regions with a high degree of inhomogeneity. These more accurate results acquired using Monte Carlo simulation however, often require orders of magnitude more calculation time so as to attain high precision, thereby reducing its utility within the clinical environment. This work aims to improve the utility of Monte Carlo simulation within the clinical environment by developing techniques which enable faster Monte Carlo simulation of radiotherapy geometries. This is achieved principally through the use new high performance computing environments and simpler alternative, yet equivalent representations of complex geometries.

Firstly the use of cloud computing technology and it application to radiotherapy dose calculation is demonstrated. As with other super-computer like environments, the time to complete a simulation decreases as $1/n$ with increasing n cloud based computers performing the calculation in parallel. Unlike traditional super computer infrastructure however, there is no initial outlay of cost, only modest ongoing usage fees; the simulations described in the following are performed using this cloud computing technology. The definition of geometry within the chosen Monte Carlo simulation environment - Geometry & Tracking 4 (GEANT4) in this case - is also addressed in this work. At the simulation implementation level, a new computer aided design interface is presented for use with GEANT4 enabling direct coupling between manufactured parts and their

equivalent in the simulation environment, which is of particular importance when defining linear accelerator treatment head geometry. Further, a new technique for navigating tessellated or meshed geometries is described, allowing for up to 3 orders of magnitude performance improvement with the use of tetrahedral meshes in place of complex triangular surface meshes. The technique has application in the definition of both mechanical parts in a geometry as well as patient geometry.

Static patient CT datasets like those found in typical radiotherapy treatment plans are often very large and present a significant performance penalty on a Monte Carlo simulation. By extracting the regions of interest in a radiotherapy treatment plan, and representing them in a mesh based form similar to those used in computer aided design, the above mentioned optimisation techniques can be used so as to reduce the time required to navigation the patient geometry in the simulation environment. Results presented in this work show that these equivalent yet much simplified patient geometry representations enable significant performance improvements over simulations that consider raw CT datasets alone. Furthermore, this mesh based representation allows for direct manipulation of the geometry enabling motion augmentation for time dependant dose calculation for example. Finally, an experimental dosimetry technique is described which allows the validation of time dependant Monte Carlo simulation, like the ones made possible by the afore mentioned patient geometry definition. A bespoke organic plastic scintillator dose rate meter is embedded in a gel dosimeter thereby enabling simultaneous 3D dose distribution and dose rate measurement.

This work demonstrates the effectiveness of applying alternative and equivalent geometry definitions to complex geometries for the purposes of Monte Carlo simulation performance improvement. Additionally, these alternative geometry definitions allow for manipulations to be performed on otherwise static and rigid geometry.

Acknowledgements

Firstly I would like to thank my project supervisors Prof. Christian Langton and Dr. Jamie Trapp for their patient and continued support throughout the realisation this work. Both always prompt when it comes to sorting out drafts and the like, always approachable when I have needed help and very supportive of my sometimes wandering scientific interests in the pursuit of what research is enjoyable and ultimately what research ends up working out.

Over the course of the last three years, Dr. Tanya Kairn, Mr. John Kenny, and Mr. Greg Pedrazzini have all been particularly helpful when experimental measurements have been required; and extremely patient when the measurements didn't work (mainly due to me). I thank them all and their colleagues at Premion for their invaluable assistance. Additionally I would like to thank Dr. Basim Kakakhel for his help in the lab when we had to prepare for the aforementioned experiments.

My friends and family have collectively supported me greatly over the course of my studies. In particular, my parents Paula and Mark Poole whom have both been exceptionally understanding and encouraging; support which has been invaluable.

Finally, I would like to direct special thanks towards Dr. Iwan Cornelius who has served as somewhat of a science role model over the last two years or so; I am very grateful for his support and friendship.

Contents

List of Publications

Manuscripts that make up the work described herein:

- *Radiotherapy Monte Carlo simulation using cloud computing technology*; **CM Poole**, I Cornelius, JV Trapp and CM Langton; Submitted to Australasian Physical & and Engineering Sciences in Medicine, August 2012
- *A CAD interface for GEANT4*; **CM Poole**, I Cornelius, JV Trapp and CM Langton; Accepted to Australasian Physical & and Engineering Sciences in Medicine, August 2012
- *Fast tessellated solid navigation in GEANT4*; **CM Poole**, I Cornelius, JV Trapp and CM Langton; Accepted to IEEE Transactions on Nuclear Science, April 2012
- *Three-dimensional patient contours as geometry for Monte Carlo simulation*; **CM Poole**, I Cornelius, JV Trapp and CM Langton; To be submitted to Medical Physics
- *A hybrid radiation detector for simultaneous spatial and temporal dosimetry*; **CM Poole**, JV Trapp, J Kenny, T Kairn, K Williams, M Taylor, R Franich and CM Langton; Accepted to Australasian Physical & and Engineering Sciences in Medicine, June 2011

Conference presentations by the author during the PhD candidature:

- *Robotic tracking of tumor movement during radiotherapy*; **CM Poole**, JV Trapp, AF Fielding and CM Langton; Oral Presentation at the Australia-Canada Prostate Cancer Research Alliance International Conference, August 2010
- *Improved prostate volume targeting during radiotherapy by robotic 4D ultrasound image guidance*; **CM Poole**, JV Trapp, CM Langton; Poster Presentation at the Prostate Cancer Foundation of Australia International Conference, August 2010

- *Vectorised DICOM-RT Regions of Interest as G4Tessellatedsolids*; **CM Poole**, I Cornelius, JV Trapp and CM Langton; Awarded Best Oral Presentation at the 1^{st} GEANT4 Australia School and User Workshop, April 2011

Other works contributed to by the author during the PhD candidature:

- *Rayleigh theory of ultrasound scattering applied to liquid-filled contrast nanoparticles*; MB Flegg, **CM Poole**, AK Whittaker, I Keen and CM Langton; Accepted to Physics in Medicine and Biology, April 2010
- *"Commissioning of a GEANT4 based treatment plan simulation tool: linac model and DICOM-RT interface"*; I Cornelius, B Hill, N Middlebrook, **CM Poole**, B Oborn and CM Langton; Submitted to Australasian Physical & and Engineering Sciences in Medicine, October 2011

List of Figures

Chapter 1

Introduction

As radiotherapy treatment delivery becomes more complex, Monte Carlo simulation becomes more useful in calculating the dose delivered to the patient. It offers a high degree of flexibility in geometry and physical process definition, as well as higher accuracy when compared to fast analytical techniques typically found in modern radiotherapy treatment planning systems. Additionally, Monte Carlo when used for radiation transport is an embarrassingly parallel computational problem, meaning many particle histories can be simulated at the same time without regard for each other; therefore supercomputers and the like are an ideal host for performing such simulations. Monte Carlo simulation of radiotherapy treatments in the clinical environment however, is not routine. The main reason for this is that the simulations themselves are very slow, and as a simulation and its geometry becomes more complex, the time required to perform the simulation increases still.

The aim of this thesis is to develop techniques for faster Monte Carlo simulation of radiotherapy geometries, including the patient and the linear accelerator treatment head. Several options are available when seeking to eliminate the requirement for long simulation times; gain access to supercomputer-like infrastructure from within the clinical environment, optimise the software used to perform the simulation, or redefine complex geometries in a manner that is equivalent

and requires less time to simulate. Alternatively, one may consider reducing the required simulation time by accepting output that is less precise, or more noisy.

Firstly background material is provided in Chapter 2 on both the topics of radiotherapy and Monte Carlo modelling for the purposes of dose calculation. The Geometry and Tracking 4 (GEANT4) Monte Carlo software toolkit is also described as it is toolkit selected in aide of carrying out this work. Techniques that improve the performance of Monte Carlo simulations applied to radiation transport are also discussed.

In Chapter 3 a technique is presented which allows for vast computing resources may be harnessed for the purposes of clinical treatment plan verification using Monte Carlo simulation and GEANT4 in particular. Cloud computing resources provided by the Amazon elastic compute cloud are used to validate treatment plans delivered by a Varian linear accelerator as a demonstration of effectiveness. Indeed the simulations described in Chapters 4 through 6 use this very technique. Technical and implementation details are presented, and the performance of the cloud computer technique evaluated.

Technical limitations concerning the definition of geometry within the GEANT4 simulation environment are addressed in Chapters 4 and 5. Specifically, in Chapter 4 we demonstrate a technique whereby geometry created using computer aided design (CAD) software can be directly loaded into GEANT4, thereby enabling accurate replication of experimental geometries in the simulation environment. Conceptually, this technique enables a direct coupling between a manufactured part and its representation in the simulation. Further in Chapter 5, computational performance issues concerning navigation of tessellated solids in GEANT4 are examined. Re-meshing tessellated triangular surfaces as a collection of individual tetrahedrons is evaluated in terms of total simulation time and geometric equivalence and found to offer significant geometry navigation performance improvments. There is particular emphasis on application to the simulation of patient anatomy derived from static computed tomography datasets; a technique

which is described further in Chapter 6.

In Chapter 6 an alternative patient geometry and anatomy description in the simulation environment using tetrahedral represenatations of DICOM regions of interest is shown, which allows for significantly faster geometry navigation when compared to using raw voxelised CT datasets. The manipulation and augmentation of otherwise static datasets with motion information is a secondary benefit of the technique. This alternative geometry description leverages the techniques described in Chapters 4 and 5 yielding a simulation of a typical radiotherapy treatment plan in less than one twentieth of the time otherwise required when using a raw CT dataset alone.

Finally, dose measurements with both spatial distribution and a temporal component are demonstrated in Chapter 7. Using a custom designed and built radiation dose rate detector, we show that dose rate history can be measured along with 3D dose distributions with the coupling of a polymer gel dosimeter and a plastic scintillator dosimeter. The technology described allows for the potential experimental validation of the 4D simulation techniques described in Chapter 6.

1.1 Objectives

The following summarises the objectives achieved by the work described here within:

Objective A: Fast Monte Carlo dose calculations without super-compute infrastructure

- Leverage cloud computing resources to expedite Monte Carlo simulations without dependency on super computing hardware

- Explore advantages of this technique over dedicated hardware

Objective B: Link experiment and simulation with accurate and precise geometry definition

- Mapping between CAD geometry and a `G4TessellatedSolid` in GEANT4
- Evaluate benefit of direct import versus conventional methods
- Automatic CAD file import for arbitrary tessellated meshes

Objective C: Improve geometry navigation performance in GEANT4 for irregular solids

- Tetrahedralise tessellated meshes and measure equivalence to standard geometry definitions
- Measure performance when taking advantage of `smart-voxels` in GEANT4
- Automatic and user-transparent tetrahedralisation of tessellated surface geometries in GEANT4
- Allow for nested tessellated solids as tetrahedral meshes in GEANT4

Objective D: Alternative patient geometry definitions augmented with 4D ultrasound for the purposes of dose calculation

- Load regions of interested defined in DICOM-RT as patient geometry in GEANT4
- Calculate geometry equivalence for dose given a configuration of fields that describe a radiotherapy treatment plan
- Perform time dependent dose calculations for radiotherapy treatment plans with target motion described by data

Objective E: Simultaneous 3D dose distribution and temporal dose rate measurements - 4D dosimetry

- Design and build an organic plastic scintillator dose-rate meter
- Calibrate the dose-rate meter for absolute dose and dose-rate
- Measure dose perturbation in a polymer gel dosimeter from the presence of a plastic scintillator
- Calibrate a polymer gel dosimeter for absolute dose using an organic plastic scintillator within the gel

Chapter 2

Literature Review

In this Chapter background material is provided, focusing on the general principals of radiotherapy, treatment planning and Monte Carlo simulation for dose calculation.

2.1 Radiotherapy

Radiotherapy is a curative, and on occasion a palliative medical technique used for the treatment of malignant tumours and suppression of immune system with ionising radiation [1, 2]. The term is used to indicate the use of high energy (4-25 MV) photons for the purposes of treatment; however other therapies such as proton therapy, electron therapy, heavy ion therapy, kV x-rays beams and brachytherapy are all forms of radiotherapy. Principally the goal is to effect double-strand breaks on the DNA molecule within the nucleus of the cells comprising the target volume, thus triggering apoptosis; programmed cell death [2,3]. In general a course of radiotherapy is divided into fractions, where many fractions may be delivered over a period of weeks. The process of fractionation as it is termed allows for high doses to be accumulated over time whilst allowing for natural repair of damaged healthy tissues.

With the use of a clinical linear accelerator, a very high (2 Gray per fraction)

and conformal dose of radiation is delivered to the target volume with surrounding critical and radio-sensitive structures spared, accordingly the radiation dose prescription indicates a minimum required dose to the target and a maximum allowable dose to specific critical structures. Actioning of the dose prescription requires a great deal of preparation on the part of the clinic including but not limited to: comprehensive treatment planning using a modern treatment planing system (TPS), treatment plan verification using hand calculations or Monte Carlo simulation and patient specific quality assurance measurement. Modern techniques, with particular reference to external beam radiotherapy (EBRT), accomplish highly conformal dose delivery to the target with intensity modulation of the beam as is the case for intensity modulated radiotherapy (IMRT) and target localisation and tracking pre-, post- and during treatment, as is the case for image guided radiotherapy (IGRT) [2,3].

2.1.1 Treatment Planning

Treatment planning is the process whereby beams or fields of radiation are configured such that the dose prescription can be satisfied [4,5]. The treatment plan itself includes specific configuration directives for execution by a clinical linear accelerator as well as contoured patient anatomy defined by the clinician [6], and the dose prescription itself described in the form of dose volume histograms and spatial dose distributions. Directives defining the sequence of field delivery and execution are represented as control-points within the DICOM-RT treatment plan; for an IMRT treatment, each modulated field from a single position may contain over 100 control points defining each beamlet that describes the final modulated field. Numerous analytical dose calculation algorithms have been made available by a variety of treatment planning system vendors. Analytical solutions are generally very fast and provide results which are comparable to those produced using Monte Carlo simulations and generally agree with mea-

surement. Prior to the treatment plan dose distribution calculation, regions of interest within the patient CT dataset are delineated. Usually the regions of interest are limited to the target volume and surrounding critical structures - often the treatment planning system will use these contours to fit conformal beams to the target volume whilst shielding other contoured regions.

2.1.2 The Varian Linear Accelerator

External beam radiotherapy using high energy photons is performed with a clinical linear accelerator. In broad terms, the linear accelerator is comprised of an electron source, accelerated wave-guide and treatment head fixed to a gantry with a 360° range of motion in the vertical plane. Within the treatment head is positioned a usually copper-tungsten alloy electron target for the production of forward scattered bremsstrahlung photons which subsequently bombard a copper flattening filter. The flattening filter to used to achieve a flat dose profile in a tank of water under specific reference conditions [2, 3].

For the Varian linear accelerator modeled for the work in this thesis, beam shaping takes place within the treatment head using a series of collimators, see figure 2.1. A ring of lead with a conical aperture, the primary collimator, effects initial collimation of the bremsstrahlung photon beam before the photons bombard the flattening filter. Orthogonal adjustable jaws positioned after the flattening filter define the square field size usually over a range of 40 cm to < 3 cm; generally these jaws are fixed for the time the beam is on. Finally, irregular shaping of the beam is performed with a multi-leaf collimator, where independent control of each leaf allows for complex outlines to be defined - the multi-leaf collimator can be controlled whilst the beam is on, as is the case for IMRT [2, 3].

Patient setup is such at the target volume is at or around the iso-center of the linear accelerator - the virtual point in space at which linear accelerator gantry

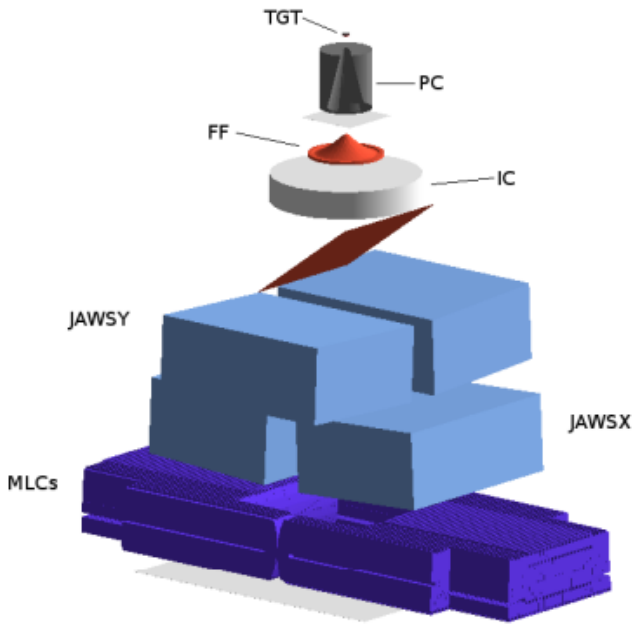

Figure 2.1: Geometry of the 6 MV Varian R iX clinac used in simulations including: target (TGT), primary collimator (PC), flattening filter (FF), ionisation chamber (IC), upper jaws in y direction (JAWSY), lower jaws in x direction (JAWSX), multi-leaf collimator (MLCs). Image courtesy of Dr. Iwan Cornelius (QUT)

rotates, usually 100 *cm* from the source [2,3]. The treatment couch with 3 degrees of freedom, and in some cases, 6 degrees of freedom with the addition of pitch and yaw type motions, enables accurate and precise positioning of the patient around the iso-center. Access around the couch is such that the treatment head can be rotated around it without interference; the surface of the couch is usually carbon fibre so as to lower its potential as a source of scattered radiation.

2.2 Monte Carlo for Radiation Transport

The Monte Carlo method is the repeated sampling of distributions that describe stochastic processes which results in a random walk through a state-space. Coupled with a ray-tracer, Monte Carlo is used for radiation transport and the simulation of the passage of particles through matter. In this case the distributions

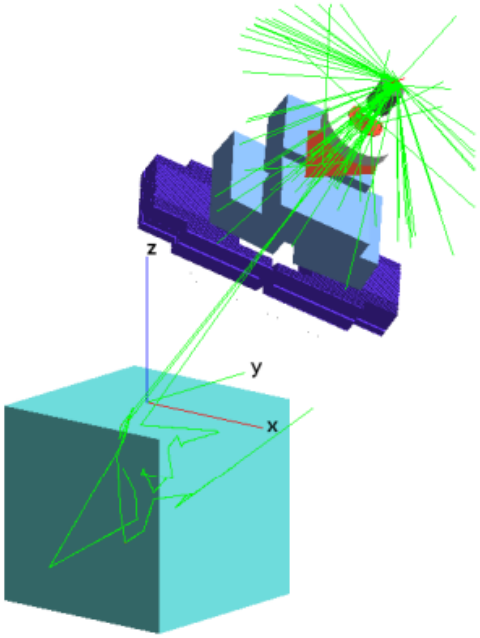

Figure 2.2: Positive gantry and collimator rotation in the IEC coordinate system, room coordinate system is indicated. Image courtesy of Dr. Iwan Cornelius (QUT).

that are sampled are interaction cross-sections for media which describe for example the production of secondary particles and scattering events and processes. A particle of interest may be from a source in a direction governed by some distribution characterised by the source type at which point it will proceed to traverse a geometry. The next interaction the particle may undergo is dependant on its type and the current media it is contained within. This interaction may occur as the particle crosses the boundary from one volume to an other, or at a predefined interval or step length. Of course, the interaction at some point may be null and the particle continues on its current path, or the interaction may strip the particle of some of its energy, and secondaries particles may be procured. In the case of secondary particle production, this particles will continue to be tracked through the geometry in a similar manner to the primary particle.

For improved accuracy, the underlying physical processes require more exacting definition and for improved precision, more particle histories must be simulated. It is the requirement to simulation more particle histories that results in

long computation time in order to acquire more accurate results.

Many software applications and programming libraries exist for this purpose [7–13], with the most widely used application in radiotherapy and medical physics being the BEAMnrc and DOSxyznrx combination based on Electron Gamma Shower (EGS) [10]. Every tool in this application space has its own feature sets, algorithm implementations and performance characteristics.

Geometry and Tracking 4 (GEANT4) is the Monte Carlo toolkit selected for this work. Compared to other Monte Carlo toolkits and software applications, it offers the highest degree of flexibility when exploring novel performance enhancement techniques as it is a developers toolkit, designed as the foundation of Monte Carlo software applications, not an application in and of itself.

2.2.1 Geometry & Tracking 4 (GEANT4)

Increasingly, GEANT4 [7,8] is being used as a tool for Monte Carlo simulation of clinical linear accelerators and the verification of radiotherapy patient treatment plans [14–16]. Photo-nuclear interactions and other features more commonly used for high energy physics Monte Carlo simulations are also available within the GEANT4 toolkit; these features are widely used in particle physics and space physics centres around the world.

Geometry Definition

Geometry definition in GEANT4 is hierarchical with a number of step required before some object can be considered defined within the overall geometry. At the upper level, the `G4GeometryManager` provides access to the geometry within the simulation environment and allows for geometry optimisations to be performed. Users seeking to define some object must first create a `G4Solid`; an object with shape but without a position within the geometry. Common solids such as `G4Box` and `G4Orb` are available to the user as well as more complex solids

such as `G4TessellatedSolid` which allow for the definition of irregular shapes or solids derived from CAD models for example [17, 18], see chapter 4. Logical geometry hierarchy such as mother-daughter relations are ascribed through the `G4LogicalVolume` class, in addition to this, other properties such as the material of the object are defined. Enabling a volume within the geometry to act as a `G4VSensitiveDetector` is also established at the logical volume level. Finally, the object is positioned relative to its mother volume with a initialisation of a `G4VPhysicalVolme`.

Tessellated Solid Navigation

Every step, at a boundary crossing or forced step governed by the setting of a maximum step length, the GEANT4 navigator determines the current step position relative to the user geometry - if the step is on the surface of a volume, or within a volume for example. For primitives such as cubes, spheres, tetrahedra and others, the determination of position within the volume is $O(1)$, that is to say the computation time required is constant and independent of the size of the volume described by the primitive. Being *primitive* is what gives rise to this property; the volume is well defined and has a specific and expected arrangement facets. Consider a rectangular prism made up of exactly six faces and eight vertexes, where opposite faces are parallel and adjacent faces are perpendicular; verifying if an arbitrary point is inside or outside of this prism is a trivial application of minimum and maximum bounds in the x, y, and z directions (assuming of course the prism has not been rotated). For a sphere, a similar operation may be applied, however the bound is applied in the radial direction.

Complex geometries may be too difficult to define with primitives alone; the tessellated solid was introduced to facilitate the definition of CAD derived surface meshes. Results presented in chapter 5 show that the time required to navigate a tessellated solid however is $O(n)$; linearly proportional to the number of facets that define the tessellated solid. Inspection of the GEANT4 source code defining

the process of inside determination for a tessellated solid shows that it is a multi-step process requiring the iteration of each facet defining the solid. Firstly, a simple bounding box check is performed, if the step is outside of the bounding box, there is certainty the step is not within the tessellated solid and the function exits. Next, each facet is tested and compared to the current step position, if there distance to the facet is within a threshold, the step is considered on the volume surface and the function exits. Finally, if the previous checks fail, 20 random rays are projected from the current step point; each facet is again looped over and tested if a ray intersects it. The direction of the intersection for the first facet crossed by a ray is determined by examining the normal vector of the facet, for a normal vector of $0 < \theta < \pi/2$ the ray is exiting the solid or if the normal vector is $\pi/2 < \theta < \pi$ the ray is entering the solid; note that each facet for the tessellated solid must be defined with its vertexes ordered in an anti-clockwise direction such that the normal for the face is pointing to the inside of the solid.

Following this, it would be expected that a geometry made up exclusively of primitives would be faster to navigate compared to one that is made up of many tessellated solids - especially if the tessellated solids are themselves defined by many facets.

Smart Voxelisation

Smart voxelisation is an automatic partitioning of the user geometry where groupings of nearby and smaller volumes are assigned to a common local virtual mother volume [8, 19]. Each virtual mother volume is referred to as a smartvoxel, and enables the GEANT4 geometry navigator to only consider volumes within the current smart voxel when determining which volume the current step is within. For geometries made up of many volumes, this technique can present significant performance improvements, however for large complex volumes such as boolean solids or tessellated solids these performance improvements will not be realised, as smart voxelisation does not apply to the navigation within a volume itself.

A Simulation

A simulation proper in GEANT4 is a combination of a number of modules or more specifically C++ classes, inheriting functionality from base classes within the toolkit [7, 8]. The most basic of simulations requires a detector construction, physics list and primary generator. Within the user detector constructions the experimental world is defined, all user geometry positioned, and detectors created. All particles and physics processes applicable to a given simulation are defined in the physics list, standard processes such as Compton scatter may be assigned to particular particles, or custom user processes created. Finally, an initial source of particles is created with the primary generator action, the generator may take the form of a point source, surface, volume or otherwise - many sources may be positioned within the geometry and repositioned in a time-dependant fashion [7, 8].

2.2.2 Computational Performance

Monte Carlo simulation is an inherently time consuming task as it requires a comprehensive calculation of all iterations a particle will undergo as it traverses a geometry. This is then compounded by the requirement that many individual particles are simulated in order to obtain precise results; increasing the required simulation time further still. The perceived slowness of a given Monte Carlo simulation can be addressed in a number of ways:

- improve the implementation of the chosen Monte Carlo technique in software, that is to say make the most of the available CPU time by avoiding unnecessary or suboptimal computations,
- run a simulation in parallel using more of the same or similar computing hardware,
- simplify the geometry so it requires less computation to navigation, reducing

the total number of volumes in the geometry for example,

- pre-compute calculations that are repeated often as part of the simulation,
- use alternative computing hardware that is optimised for the kinds of calculations that are performed using Monte Carlo, graphics processing units (GPU) for example.

A number of algorithms have been presented by others which allow for significantly improved Monte Carlo simulation performance when considering radiation transport [20–24]. In general these algorithms are either a change to the way the simulation geometry is represented such as the smart voxelistation algorithm in GEANT4 described previously, or require pre-computing parts of the simulation that are performed often and produce the same or similar result. Superposition Monte Carlo is a good example of using pre-computed data for simulation acceleration [22, 23]. An electron track kernel is calculated for a primary interaction which saves all of the iterations secondary particles will under go about a primary interaction site, these tracks are then replayed for each primary interaction without the need to recalculate each track.

2.3 Motivation

In this Chapter the Monte Carlo method applied to radiation transport and the simulation of radiotherapy treatments has been examined. Whilst others have presented techniques to reduce the computational burden of Monte Carlo simulation, there is much room for improvement especially when considering irregular geometry such as patient anatomy. This thesis explores cloud computing as an alternative to traditional computing platforms for Monte Carlo simulation, as well as develops new geometry definitions for simulation acceleration.

Bibliography

[1] S H Levitt, J A Purdy, C A Perez, and S Vijayakumar. *Technical Basis of Radiation Therapy*. Springer-Verlah, Berlin, Heidelberg, 2006.

[2] P. Metcalfe, T. Kron, and P. Hoban. *The physics of radiotherapy X-rays and electrons*. Medical Physics Pub., 2007.

[3] F.M. Khan. *The physics of radiation therapy*. 2003.

[4] J.E. Munzenrider, M. Pilepich, J.B. Rene-Ferrero, I. Tchakarova, and B.L. Carter. Use of body scanner in radiotherapy treatment planning. *Cancer*, 40(1):170–179, 1977.

[5] P. Hobday, N.J. Hodson, J. Husband, R.P. Parker, and J.S. Macdonald. Computed tomography applied to radiotherapy treatment planning: techniques and results. *Radiology*, 133(2):477, 1979.

[6] C. Fiorino, M. Reni, A. Bolognesi, G.M. Cattaneo, and R. Calandrino. Intra- and inter-observer variability in contouring prostate and seminal vesicles: implications for conformal treatment planning. *Radiotherapy and oncology*, 47(3):285–292, 1998.

[7] J. Allison, K. Amako, J. Apostolakis, H. Araujo, P.A. Dubois, M. Asai, G. Barrand, R. Capra, S. Chauvie, R. Chytracek, et al. Geant4 developments and applications. *IEEE Trans. Nucl. Sci.*, 53(1):270–278, 2006.

[8] S. Agostinelli, J. Allison, K. Amako, J. Apostolakis, H. Araujo, P. Arce, M. Asai, D. Axen, S. Banerjee, G. Barrand, et al. Geant4 simulation toolkit. *Nuclear Instruments and Methods in Physics Research-Section A Only*, 506(3):250–303, 2003.

[9] DWO Rogers, B. Walters, I. Kawrakow, et al. Beamnrc users manual. *NRC Report PIRS*, 509, 2006.

[10] W.R. Nelson, H. Hirayama, and D.W.O. Rogers. Egs4 code system. Technical report, Stanford Linear Accelerator Center, Menlo Park, CA (USA), 1985.

[11] F. Salvat, J.M. Fernández-Varea, and J. Sempau. Penelope-2006: A code system for monte carlo simulation of electron and photon transport. In *Workshop Proceedings Barcelona, Spain*, volume 4. Citeseer, 2006.

[12] J.F. Briesmeister and Los Alamos National Laboratory. *MCNP–A general Monte Carlo code for neutron and photon transport*. Los Alamos National Laboratory, 1986.

[13] H. Hirayama, Y. Namito, W.R. Nelson, A.F. Bielajew, S.J. Wilderman, and U. Michigan. *The EGS5 code system*. United States. Dept. of Energy, 2005.

[14] S. Jan, D. Benoit, E. Becheva, T. Carlier, F. Cassol, P. Descourt, T. Frisson, L. Grevillot, L. Guigues, L. Maigne, et al. GATE V6: a major enhancement of the GATE simulation platform enabling modelling of CT and radiotherapy. *Physics in Medicine and Biology*, 56:881–901, 2011.

[15] B. Caccia, C. Andenna, and G. A. P. Cirrone. MedLinac2: a GEANT4 based software package for radiotherapy. *Annali dell'Istituto superiore di sanità*, 46:173–177, 2010.

[16] L. Grevillot, T. Frisson, D. Maneval, N. Zahra, J. N. Badel, and D. Sarrut. Simulation of a 6 MV Elekta Precise Linac photon beam using GATE/GEANT4. *Physics in Medicine and Biology*, 56:903–918, 2011.

[17] M. Constantin, D. E. Constantin, P. J. Keall, A. Narula, M. Svatos, and J. Perl. Linking computer-aided design (CAD) to Geant4-based Monte Carlo simulations for precise implementation of complex treatment head geometries. *Physics in Medicine and Biology*, 55:N211–N220, 2010.

[18] T. Beutier, E. Delage, M. Wouts, O. Serres, and P.F. Peyrard. Fastrad new tool for radiation prediction. In *Proceedings of the 7th European Conference on Radiation and Its Effects on Components and Systems, 2003. RADECS 2003.*, pages 181–183, 2003.

[19] G. Cosmo. The geant4 geometry modeler. In *Nuclear Science Symposium Conference Record, 2004 IEEE*, volume 4, pages 2196–2198. IEEE, 2004.

[20] J. Sempau, S.J. Wilderman, and A.F. Bielajew. Dpm, a fast, accurate monte carlo code optimized for photon and electron radiotherapy treatment planning dose calculations. *Physics in medicine and biology*, 45:2263, 2000.

[21] I. Kawrakow et al. Vmc++, electron and photon monte carlo calculations optimized for radiation treatment planning. In *Advanced Monte Carlo for Radiation Physics, Particle Transport Simulation and Applications: Proc. Monte Carlo 2000 Meeting*, pages 229–236. Berlin: Springer, 2001.

[22] P.J. Keall and P.W. Hoban. Superposition dose calculation incorporating monte carlo generated electron track kernels. *Medical physics*, 23:479, 1996.

[23] PJ Keall, PW Hoban, and MP West. Super-monte carlo: A photon/electron dose calculation algorithm for radiotherapy. *Radiation Physics and Chemistry*, 53(3):275–281, 1998.

[24] CM Ma, T. Pawlicki, JS Li, SB Jiang, J. Deng, A. Kapur, E. Mok, G. Luxton, and AL Boyer. Mcdosea dose calculation tool for radiotherapy treatment planning. *Med. Phys*, 26:1148, 1999.

Chapter 3

Radiotherapy Monte Carlo simulation using cloud computing technology

Target Journal

Australasian Physical & and Engineering Sciences in Medicine

Publication Status

Submitted, August 2012.

Authors

CM Poole[1,2] *(Candidate)*, I Cornelius[1], JV Trapp[1,†] and CM Langton[1,⋆]

[1] School of Chemistry, Physics and Mechanical Engineering, Science and Engineering Faculty, Queensland University of Technology
[2] Cancer Care Services, Royal Brisbane & Womens Hospital

⋆ Supervisor
† Associate supervisor

Statement of Joint Authorship

CMP conceived the overall concept, developed proof of concept software and wrote the paper. IC assisted in software development and

testing. IC, JVT and CML assisted CMP in design, scientific development process and manuscript editing.

Abstract

Cloud computing allows for vast computational resources to be leveraged quickly and easily in bursts as and when required. Here we describe a technique that allows for Monte Carlo radiotherapy dose calculations to be performed using GEANT4 and executed in the cloud, with relative simulation cost and completion time evaluated as a function of instance count. As expected, simulation completion time decreases as $1/n$ for n parallel instances and relative simulation cost is found to be optimal where n is a factor of the total simulation time in hours. Using the technique, we demonstrate the potential usefulness of cloud computing as a solution for rapid Monte Carlo simulation for radiotherapy dose calculation without the need for dedicated local computer hardware as a proof of principal.

3.1 Introduction

Significant computational overhead prevents the routine use of Monte Carlo simulation applied to radiotherapy problems in the clinical setting, generally as a consequence of limited access to suitable computing hardware. The advent of cloud computing however provides a low cost and easy to maintain alternative to the set-up of dedicated computing hardware in the clinic [1]. Indeed, several authors have explored the usefulness of "the cloud" for Monte Carlo simulation [2–5], the most notable of which uses Fluka [6] for proton beam dose calculations on the Amazon Elastic Compute Cloud (EC2, Amazon Web Services LLC, USA) [1]. This work too uses EC2 as the host cloud computing platform, however Geometry and Tracking 4 (GEANT4) has been selected to simulate a clinical radiotherapy linear accelerator. Here we aim to show the immediate capability of the cloud for the purpose of radiotherapy Monte Carlo simulation whilst within the clinical environment.

GEANT4 is a C++ toolkit for the simulation of particle transport through geometry and is the Monte Carlo toolkit selected to carry out this work. It is used widely in the field of high energy physics [7] and sees increasing adoption for radiotherapy treatment simulation [7–12]. Flexible geometry definition and physics process customisation provides the user with a high level of control, and the opportunity to simulate a wide range of radiotherapy techniques including brachytherapy, hadrontherapy and intensity modulated radiotherapy [13]. Additionally, as it is a developers toolkit it is an ideal platform for experimenting with new parallelization techniques and simulation hosts such as cloud computing platforms.

Cloud computing is the use of virtual and remote computer hardware for the purposes of scalable service provision such as high demand web-hosting with volatile loading conditions and scientific computation problems requiring significant and variable computer or memory resources [14–16]. This sounds very much

like the typical function of super computer clusters where a fixed number nodes may be configured to perform many possible functions, and resources are allocated based on job priority. The cloud computing paradigm however, differs from this fix-resource model to one enables the number of nodes in the cluster to expand and contract dynamically based on demand. This is accomplished with the use of nodes or instances that are usually configured and booted once to perform a single task before being shutdown again ready to accept a new configuration. The advantage of this is that many similar nodes can be launched simultaneously to perform a single task in parallel. And as these instances are virtual, the configuration is not limited to software, hardware configurations can be performed too, with the tuning of RAM, CPU power and disk storage space for example.

For this study, EC2 provides scalable computing instances and the S3 provides the off-instances data storage area. Compute capability of a particular AWS instance type is described using the EC2 compute unit, where one compute unit is the equivalent CPU capacity of a 1.0-1.2 GHz 2007 Opteron or 2007 Xeon processor [17]. At creation, any EC2 instance may have custom user data parsed to it, the user data itself may take on any form whether it be binary, ASCII or otherwise - subsequently this user data may be used to uniquely configure running tasks on the instances. Two modes of access are available to the users, on-demand instance creation billed at a fixed hourly rate, or a variable rate where the use may bid for unused instances with the time to availability may vary depending on current demand – this is known as the spot market. Access to the resources provided by AWS cloud services such as EC2 and Amazon simple storage solution (S3) and the cloud services provided by other vendors can be performed programatically using the *boto* Python module [18].

Herein we describe in the process of executing a pre-existing GEANT4 simulation of a clinical linear accelerator [19] on the Amazon EC2 computing resource. The method has application outside of radiotherapy and is not restricted to AWS, however a radiotherapy linear accelerator Monte Carlo simulation executed using

AWS is used here as proof of principal.

3.2 Methods

A Monte Carlo model of Varian Clinac was commissioned for dose calculation as described elsewhere [19]. Along with a Python (Python Software Foundation, USA) [20] interface to the simulation, the *boto* Python cloud computing module was used to automatically distribute jobs to the cloud environment from the local user machine.

3.2.1 AWS Instance Set-up

A single instance of type *t1.micro* was launched using the pre-built and official Ubuntu 10.04 LTS 64 bit Amazon Machine Image (AMI) with identifier *ami-3202f25b*. The boot process itself was similar to the normal boot process for a default install of any recent version of the Ubuntu server distribution [21]. Unlike a conventional local install however, the *libcloud* [22] package was installed by default on the AMI enabling access to user data parsed to the instance at the time of creation. GEANT4 version 9.3 and its dependencies were compiled and installed on the instance as well as other packages including *boost::python* and the *numpy* Numerical Python module [23]. Where available, pre-built binaries in the Ubuntu software repositories were favoured over compiling software from source. Once configured, the instance was saved as a custom and private AMI using the menu options available in the AWS dashboard. This custom AMI was then available to boot up to 20 instances with the default AWS account set-up. In the case of booting 20 High CPU Extra Large EC2 instances, 160 CPU cores were made available to the user with a total compute capability of 400 EC2 units.

3.2.2 Distributing Jobs in the Cloud

Using *boto*, the Python module for AWS including EC2 and S3, a job launcher was created that managed the packing of a job description and data into a compressed archive and the launching of a group instances, see figure 3.1. For a given job, the simulation configuration included a manifest of all files and folders to be included as job data. Using the *tarfile* Python module, part of the Python standard library [20], each file or folder in the manifest was added to an archive, followed by compression and writing to disk. From the local user machine, the compressed job archive was uploaded to S3 one time per unique simulation using *boto*. An EC2 reservation was requested which launched the prescribed number of instances for the job; a process fully managed by the *boto* Python module and EC2. Each instance had user data containing the simulation configuration including the location of the job archive on S3 transmitted to it automatically.

At instance boot time, a Python script was automatically executed, recovering the simulation configuration from the pre-transmitted user data and launching a pool of worker processes with a pool size equal to the number of processor cores available on the instance, see figure 3.2. The worker pool was created using the *multiprocessing* Python module [20], again part of the Python standard library enabling a simulation described in a Python function to be executed multiple times and concurrently across a number of processes equal to the pool size. On each instance, the master process managing the pool of worker processes, waited for all workers to finish execution, and subsequently combined and compressed the results returned by each worker process.

Finally, the compressed result was uploaded to S3 to a location specified in the simulation configuration and the instance was terminated as soon as possible, thus minimising the potential of cost escalation. Retrieving results from S3 could be performed using the AWS dashboard and a web-browser. For execution of instances on the spot market, a maximum bid price could be specified at the

time of reservation and configured as a parameter along with all other simulation parameters. From the user perspective, there was no difference between a instance acquired on-demand or bid for on the spot market.

3.2.3 Benchmarking Performance and Relative Cost

High CPU Extra Large EC2 instances were chosen for all jobs executed in the cloud as they provided the highest on-demand compute density for absolute cost. A series of test simulations were performed so as to examine simulation performance as a function of EC2 instance count. Using the GEANT4 geometry primitive *G4Box*, a 40 *cm* cubic water phantom was defined and positioned with its center at the iso-center of the linear accelerator; with a 100 *cm* source to axis distance (SAD) or 80 *cm* source to surface distance (SSD). Irradiated with a jaw defined 5×5 *cm* field and gantry and primary collimator angles set to zero, 2.5×10^6 electrons incident on the copper target in the linear accelerator treatment head were simulated. The simulation was repeated for a range of EC2 instance counts ($1 \leq n \leq 20$) on the spot market with simulation completion time (the time elapsed from starting a job to uploading a result to S3), instance uptime, total simulation time (the total real CPU time used) and total simulation cost were recorded. On-demand instance cost was calculated from the billed instance hours multiplied by the on-demand rate for the High CPU Extra Large instance type and compared to the actual cost incurred as a result of simulating the above using instances on the spot market.

3.3 Results

3.3.1 Simulation Output

Figure 3.4 shows typical output for the simulation described in section 3.2.3 using a 2 *mm* scoring dose grid. All dose values are shown normalised to the maximum

central axis dose. The size in memory for the entire dose grid with $128 \times 128 \times 128$ voxels using single precision floating point values was 8 MB per worker process for a total of 64 MB per instance.

3.3.2 Compute Performance

For the simulation described in section 3.2.3 the average time from instance boot to the start of the simulation on the same node was $59 \pm 1s$. Figure 3.3(a) shows the simulation completion time t_c as a function of instance count; it was found to follow

$$t_c = \frac{t_s}{n_i n_p}, \tag{3.1}$$

where t_s is the total simulation time required, $n_i \in \mathbb{N}^\star = \{1, 2, 3, \ldots, 20\}$ is the number of instances used per job and $n_p \in \mathbb{N}^\star = \{1, 2, 3, \ldots, 8\}$ is the number of processors available per instance. Noting that the default AWS accounts allowed for a maximum of $n_i = 20$ instances, and the maximum number of processors available per instances was $n_p = 8$ as of August 2012 [17]. Total simulation time or the total real CPU time consumed for the simulation as a function of instance count is shown in figure 3.3(b). Mean total simulation time required for the simulation described in section 3.2.3 was $t_s = 26.1 \pm 0.2$ $hours$ where the uncertainty represents one standard deviation about the mean.

3.3.3 Relative Usage Costs

Where the instance count was greater than the simulation completion time in hours, cost escalation was linear with increasing instance count, see figure 3.5. Billable instances hours required to complete a given job requiring t_s total compute hours were found to follow

$$t_i = n_i \left\lceil \frac{t_s}{n_i n_p} \right\rceil = n_i \left\lceil t_c \right\rceil, \tag{3.2}$$

where $t_i \in \mathbb{N}^\star = \{1, 2, 3, \ldots\}$ is the total billable instance hours and $\lceil \ldots \rceil$ indicates the ceiling function, noting that the uptime of a given instance was rounded up to the nearest hour for the purposes of billing. Simulations running at least total cost were found where the simulation time in hours was wholly divisible by the total number of instances running for that job, corresponding to the factors of $\lceil t_s/n_i \rceil \in \mathbb{N}^\star = \{1, 2, 3, \ldots\}$.

3.4 Discussion & Conclusion

Using a GEANT4 simulation of a clinical linear accelerator, executed on the Amazon Elastic Compute Cloud, we have demonstrated the potential usefulness of cloud computing for rapid radiotherapy dose calculation. Additionally, a simple formulation allowing for the optimal selection of instance count for least cost has been proposed, given some estimate of total simulation time required. Figure 3.3(a) shows simulation time decreasing as $1/n$ with increasing instance count as observed by others [1], cost however increases linearly with increasing instance count when simulation time in hours is less than the instance count, as shown in figure 3.3(b). For a given simulation, if time is not a critical factor, the number of instances used can be tuned for least cost by ensuring each instance is in use for whole hours, as Amazon EC2 instances charges are not prorated for partial instance hour usage. However, in an environment where time is critical, increasing instance count reduces simulation time with a linearly increasing cost penalty.

Application of this technique enables a GEANT4 user to perform a simulation in a distributed compute environment, with a low entry cost and no express need for dedicated compute hardware. For clinics in developing countries for example, which may not have sufficient resources to provide adequate cancer care [24] much less manage dedicated compute hardware, this may be of particular benefit. Indeed, the shortfall in the quality of cancer care in developing countries has been identified by others [24,25], in particular the relationship between inadequate staff

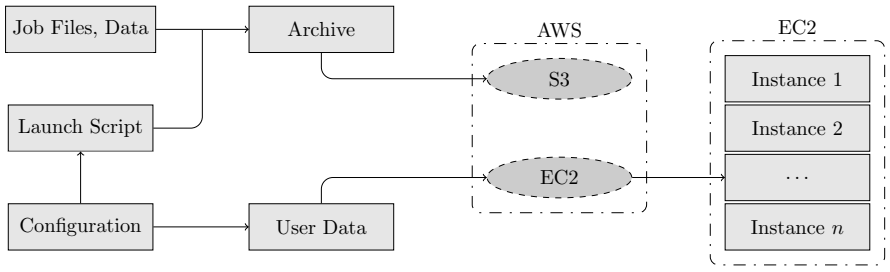

Figure 3.1: Launching EC2 instances from the local user machine.

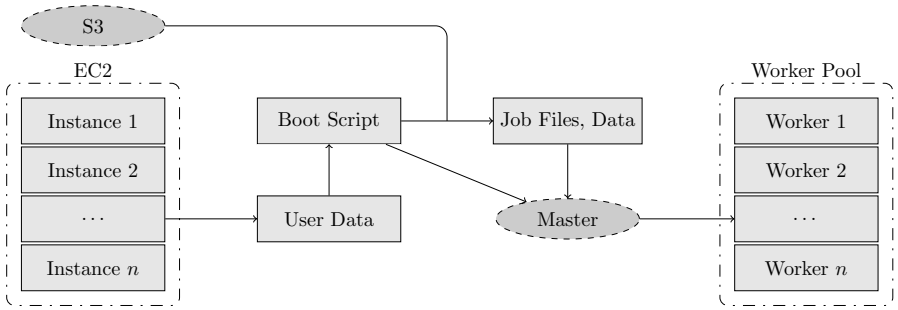

Figure 3.2: Simulation configuration and worker pool creation on each EC2 instance.

training and suboptimal treatment delivery [25]. Systems to remedy this have been proposed by others, and of particular note is the Hospital Platform for E-health (HOPE) [26] enabling the remote verification of radiotherapy treatment plans and other diagnostic and therapeutic tests. Adoption of initiatives such as HOPE, coupled with the computational resources provided by the cloud and the simulation techniques described here within may offer significant scientific and social benefit.

Presently this work is part of a software toolkit using GEANT4 for the simulation of clinical linear accelerators [19]. Source code for running GEANT4 simulations on EC2 as described here within is freely available and may be obtained from: http://code.google.com/p/manysim/

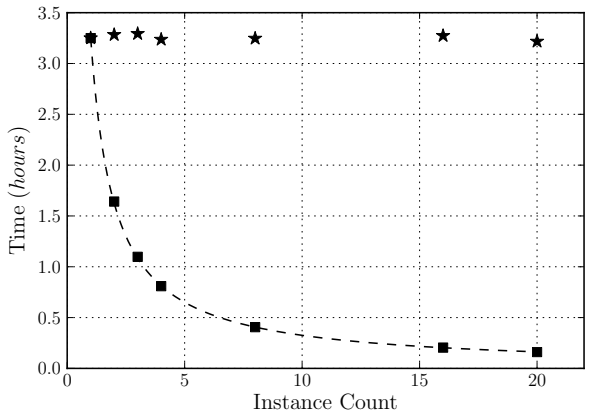

(a)

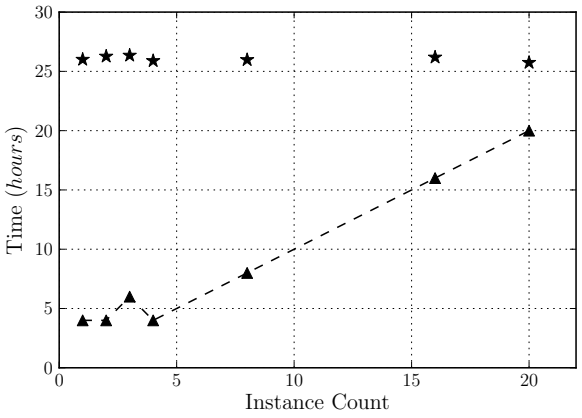

(b)

Figure 3.3: Simulation time (a) where stars indicate the total instance up-time, squares indicate the time to simulation completion and the dashed line indicates the predicted simulation completion time (equation 1). Billable instance time (b) as a function of instance count where stars indicate the total compute required, triangles indicate the billable instance time, and the dashed line indicates the predicted billable instance time (equation 2).

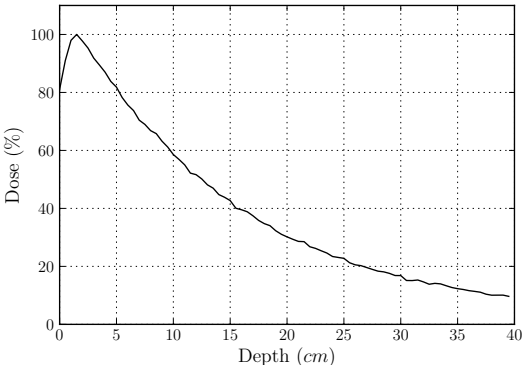

(a)

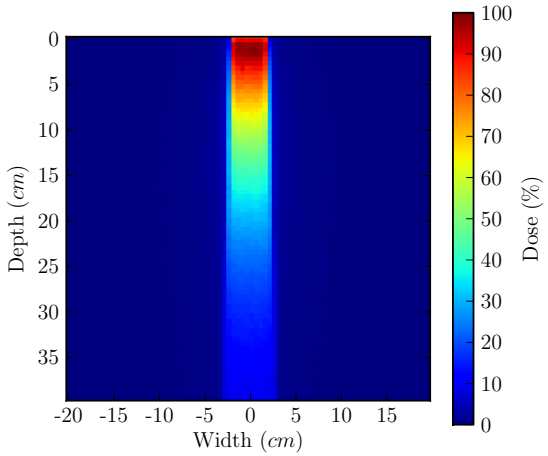

(b)

Figure 3.4: Simulation output; (a) shows the central axis depth dose and (b) shows the dose distribution of the central slice in the water phantom. Note that the iso-center of the simulated linear accelerator was positioned at (0, 20) in (b).

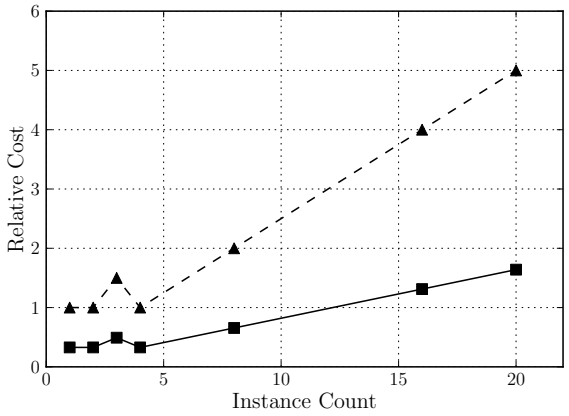

Figure 3.5: Simulation cost as a function of instance count where squares indicate the incurred cost as a result of bidding for Amazon EC2 High CPU Extra Large instances on the spot market (0.223 USD/hour), triangles indicate the equivalent cost had the on-demand rate of 0.68 USD/hour been charged, and the solid and dashed lines indicate the predicted instances hours (equation 2) multiplied by the hourly rate.

Bibliography

[1] R.W. Keyes, C. Romano, D. Arnold, and S. Luan. Radiation therapy calculations using an on-demand virtual cluster via cloud computing. *Arxiv preprint arXiv:1009.5282*, 2010.

[2] J. Gruntorad and M. Lokajicek. International Conference on Computing in High Energy and Nuclear Physics (CHEP'09). In *Journal of Physics: Conference Series*, volume 219, page 001001, 2010.

[3] A. Farbin. Emerging Computing Technologies in High Energy Physics. *Arxiv preprint arXiv:0910.3440*, 2009.

[4] A Silverman, I Fedorko, W Lapka, and G Lo Presti. CHEP 2010 Report. CHEP - Computing in High Energy and nuclear Physics. Technical Report CERN-IT-Note-2010-007, CERN, Geneva, Nov 2010.

[5] M. Constantin, D. Sawkey, S. Mansfield, and M. Svatos. Su-e-e-05: The compute cloud, a massive computing resource for patient-independent monte carlo dose calculations and other medical physics applications. *Medical Physics*, 38:3392, 2011.

[6] A. Ferrari, P.R. Sala, A. Fasso, and J. Ranft. Fluka. *CERN-library in: http://fluka. web. cern. ch/fluka*, 2005.

[7] S. Agostinelli, J. Allison, K. Amako, J. Apostolakis, H. Araujo, P. Arce, M. Asai, D. Axen, S. Banerjee, G. Barrand, et al. Geant4 - a simulation

toolkit. *Nuclear Instruments and Methods in Physics Research-Section A Only*, 506(3):250–303, 2003.

[8] B. Caccia, C. Andenna, and G. A. P. Cirrone. MedLinac2: a GEANT4 based software package for radiotherapy. *Annali dell'Istituto superiore di sanità*, 46:173–177, 2010.

[9] S. Jan, D. Benoit, E. Becheva, T. Carlier, F. Cassol, P. Descourt, T. Frisson, L. Grevillot, L. Guigues, L. Maigne, et al. GATE V6: a major enhancement of the GATE simulation platform enabling modelling of CT and radiotherapy. *Physics in Medicine and Biology*, 56:881, 2011.

[10] E. Spezi and G. Lewis. An overview of Monte Carlo treatment planning for radiotherapy. *Radiation protection dosimetry*, 2008.

[11] L. Grevillot, T. Frisson, D. Maneval, N. Zahra, J. N. Badel, and D. Sarrut. Simulation of a 6 MV Elekta Precise Linac photon beam using GATE/GEANT4. *Physics in Medicine and Biology*, 56:903, 2011.

[12] P. Rodrigues, A. Trindade, L. Peralta, C. Alves, A. Chaves, and M. C. Lopes. Application of GEANT4 radiation transport toolkit to dose calculations in anthropomorphic phantoms. *Applied Radiation and Isotopes*, 61(6):1451–1461, 2004.

[13] J. Allison, K. Amako, J. Apostolakis, H. Araujo, P.A. Dubois, M. Asai, G. Barrand, R. Capra, S. Chauvie, R. Chytracek, et al. Geant4 developments and applications. *Nuclear Science, IEEE Transactions on*, 53(1):270–278, 2006.

[14] M. Armbrust, A. Fox, R. Griffith, A.D. Joseph, R. Katz, A. Konwinski, G. Lee, D. Patterson, A. Rabkin, I. Stoica, et al. A view of cloud computing. *Communications of the ACM*, 53(4):50–58, 2010.

[15] B. Hayes. Cloud computing. *Communications of the ACM*, 51(7), 2008.

[16] M.A. Vouk. Cloud computing–issues, research and implementations. *Journal of Computing and Information Technology*, 16(4):235–246, 2004.

[17] Amazon EC2 Instance Types. Amazon Web Services LLC. http://aws.amazon.com/ec2/instance-types/, April 2011.

[18] M. Garnaat et al. *Boto Python interface to Amazon Web Services Documentation*. Computer software. http://code.google.com/p/boto/, v2.0 edition, 2010.

[19] I. Cornelius, B. Hill, N. Middlebrook, C. Poole, B. Oborn, and C. Langton. Commissioning of a Geant4 based treatment plan simulation tool: linac model and DICOM-RT interface. *Arxiv preprint arXiv:1104.5082*, April 2011.

[20] G. van Rossum and F. L. Drake. *Python Reference Manual*. Python Software Foundation. http://python.org/, v2.7.1 edition, April 2011.

[21] Ubuntu Community Documentation. https://help.ubuntu.com/community/EC2StartersGu *Ubuntu EC2 Starters Guide*, March 2011.

[22] Computer software. http://ci.apache.org/projects/libcloud/apidocs/. *Libcloud: a unified interface to the cloud*, v0.4.2 edition, 2011.

[23] D. Ascher, P.F. Dubois, K. Hinsen, J. Hugunin, T. Oliphant, et al. *Numerical Python Documentation*. Computer software. http://numpy.scipy.org/, v1.5 edition.

[24] T.P. Hanna and A.C.T. Kangolle. Cancer control in developing countries: using health data and health services research to measure and improve access, quality and efficiency. *BMC International Health and Human Rights*, 10(1):24, 2010.

[25] T.P. Shakespeare, M.F. Back, J.J. Lu, K.M. Lee, and R.K. Mukherjee. External audit of clinical practice and medical decision making in a new Asian

oncology center: results and implications for both developing and developed nations. *International Journal of Radiation Oncology* Biology* Physics*, 64(3):941–947, 2006.

[26] M. Diarena, S. Nowak, JY Boire, V. Bloch, D. Donnarieix, A. Fessy, B. Grenier, B. Irrthum, Y. Legré, L. Maigne, et al. HOPE, an open platform for medical data management on the grid. *Studies in health technology and informatics*, 138:34, 2008.

Chapter 4

A CAD interface for GEANT4

Target Journal

Australasian Physical & and Engineering Sciences in Medicine

Publication Status

Accepted for publication, August 2012

Authors

CM Poole[1,2] *(Candidate)*, I Cornelius[1], JV Trapp[1,†] and CM Langton[1,⋆]

[1] School of Chemistry, Physics and Mechanical Engineering, Science and Engineering Faculty, Queensland University of Technology
[2] Cancer Care Services, Royal Brisbane & Womens Hospital

⋆ Supervisor
† Associate supervisor

Statement of Joint Authorship

CMP conceived the overall concept, developed proof of concept software and wrote the paper. IC assisted in software development and testing. IC, JVT and CML assisted CMP in design, scientific development process and manuscript editing.

Abstract

Often CAD models already exist for parts of a geometry being simulated using GEANT4. Direct import of these CAD models into GEANT4 however, may not be possible and complex components may be difficult to define via other means. Solutions that allow for users to work around the limited support in the GEANT4 toolkit for loading predefined CAD geometries have been presented by others, however these solutions require intermediate file format conversion using commercial software. Here within we describe a technique that allows for CAD models to be directly loaded as geometry without the need for commercial software and intermediate file format conversion. Robustness of the interface was tested using a set of CAD models of various complexity; for the models used in testing, no import errors were reported and all geometry was found to be navigable by GEANT4.

4.1 Introduction

Geometry & Tracking 4 (GEANT4) is a C++ toolkit specifically designed to track particles traversing a geometry whilst being subject to physical processes [1,2], it finds application in fields such as nuclear and particle physics, space engineering, and medical physics [3–6]. Numerous physical processes can be modeled including photo-nuclear interactions, optical processes such as scintillation and Cherenkov radiation and other particle interactions over a wide energy range (250 eV up to TeV energies); the full gamut of processes available to the user is described by others [1, 2]. Fast and effective geometry definition is available to the user with constructs such as *G4Orb* for defining orbs, *G4Box* for defining rectangular prisms and the concept of boolean solids. Complex and irregular solids defined by a surface mesh can also be created using the *G4TessellatedSolid* [1,2]. Currently however, there is limited support for directly loading pre-existing or user defined computer aided design (CAD) models as geometry in GEANT4, whether it be an arrangement of primitive solids, or a surface mesh. Of the two methods available, both are reliant on intermediate file format conversion using commercial software [7,8] and can only load CAD models described using the standard for the exchange of product model data (STEP - ISO 10303) [9].

ISO standard STEP is a CAD format designed to supersede the still widely used initial graphics exchange specification (IGES) [9, 10]. As such STEP has previously been the target format for loading CAD geometry into GEANT4. The persistence example with identifier 'G02' distributed with GEANT4 describes loading STEP Tools (STEP Tools Incorporated, New York) files directly. Intermediate conversion of STEP to STEP Tools is required using the commercial ST-Viewer program or ST-Developer libraries (STEP Tools Incorporated, New York). This process, shown in Figure4.1(a) allows for assemblies of components to be loaded directly, however the STEP Tools programs and libraries may be prohibitively expensive for some users. Constantine et al [7] described the process of

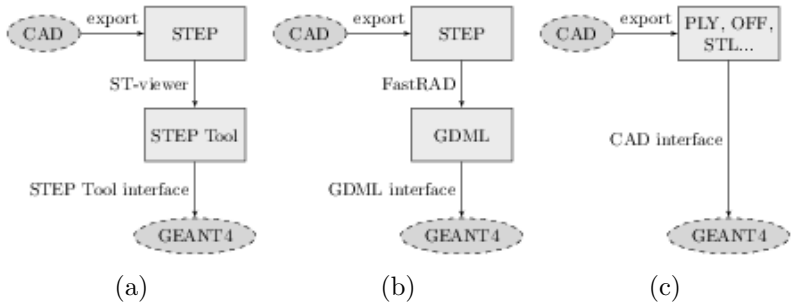

Figure 4.1: A diagrammatic comparison between two currently available CAD import techniques where (a) shows the technique described in persistence example G02, (b) shows the STEP to GDML conversion technique [7], and (c) shows the new direct import technique proposed here within.

converting STEP to geometry description mark-up language (GDML) using the commercial software FastRad (Tests & Radiation - Toulouse) [8], refer to Figure4.1(b). Functionality within the GEANT4 toolkit already allows for geometries to be saved and reloaded using GDML [11], it is based on extensible mark-up Language (XML), allowing for persistence of many aspects of the GEANT4 geometry hierarchy [11]. However, as with the method used in GEANT4 persistence example 'G02', FastRad may also be considered prohibitively expensive for some users as it has a requirement of annual licensing, in addition to this the trial version limits the conversion process to no more than 20 elements per assembly.

Loading CAD models as geometry in a GEANT4 Monte Carlo simulation is particularly useful in instances where the geometry is such that it would be difficult to define with an arrangement of primitive solids. Typical examples include the description of components in beamlines such as targets, filters and collimators and for medical applications, metallic implants such as hip prostheses and anatomical structures derived from x-ray CT scans. CAD based geometry allows for more accurate simulation based representations of an experimental setup to be attained more rapidly [7], especially if parts of the experimental setup have already been designed using CAD software. Whilst using a CAD model as geometry in GEANT4 may reduce the possibility of error when compared to manually creating a geometry in GEANT4 [7], any requirement to convert the CAD geome-

try to an intermediate file format gives rise to the potential for incorrect geometry definition, especially in instances where the source CAD geometry is undergoing regular modification and intermediate file conversion is not automated or in sync with revisions to the source CAD file.

Programming toolkits already exist for the creation and manipulation of triangular and quadrangular boundary representation (BREP) meshes; the same kinds exportable by many modern CAD packages [12–14]. Most notably the freely available templated C++ library VCGLIB (Visual Computing Laboratory, Italy) offers advanced mesh manipulation functionality and point cloud surface reconstruction algorithms. In addition to this, VCGLIB already offers an import/-export interface for many common CAD file formats [14]. Herein we describe a very simple technique that allows for BREP CAD models to be directly loaded as tessellated solids in GEANT4. The technique is capable of handling many BREP file formats exportable by CAD programs whilst not relying on intermediate file format conversions.

4.2 Methods

The GEANT4 (version GEANT4.9.5 patch 1) geometry hierarchy is divided into solids, logical volumes and physical volumes where solids describe shape, logical volumes define material properties and mother-daughter relations, and physical volumes define placement within the mother volume [1, 2]. The equivalent GEANT4 solid to a BREP geometry is the tessellated solid (*G4TessellatedSolid*) and has specific properties so as to enable correct geometry navigation by the GEANT4 kernel. In particular, the tessellated solid must describe a closed surface, that is to say the boundary between the inside and outside of the solid is defined for all points. Furthermore, all faces on this surface (whether they be triangular or quadrangular faces), must not have coincident vertexes; for example a triangular face must have exactly three unique vertexes thereby ensuring it

has an area greater than zero. When a face is added to the solid, the direction and order of the vertexes must be anti-clockwise when the normal of the face is pointing towards the inside of the volume; the GEANT4 navigator uses this convention when it determines if a point is inside or outside of the tessellated solid. For tessellated solids with face vertex order in the opposite direction, navigation errors may arise. Additionally, boolean operations can not be performed with tessellated solids.

As common BREP CAD file formats and GEANT4 tessellated solids encode a surface mesh in similar ways, a direct mapping can be achieved by iterating over all of the faces in a BREP and adding them directly to the tessellated solid in GEANT4. For a direct mapping to be effective however, vertexes and faces defined in a BREP must be accessible in a common way that is independent of the source file format. This common access to various CAD file formats is achieved here using VCGLIB. Various custom types derived from VCGLIB base classes may be defined so as to describe for example a stereo-lithography format (STL) [15] or Stanford polygon file format (PLY) [16] mesh and the elements that encode it, such as vertexes, edges and faces. Template parameters are used to attach attributes such as position for example to these custom types, in effect each custom type becomes a collection of specific VCGLIB attributes; a comprehensive description of this scheme is provided in the VCGLIB documentation [14]. Wrappers as they are referred to in VCGLIB extend the core to provide mesh manipulation functionality including importers, exporters and mesh refinement tools, generally the arguments that these wrappers expect are instances of custom types inheriting from VCGLIB base types. Here a custom VCGLIB type is defined that acts as the access layer between common CAD files and GEANT4, the process is automatic and transparent to the user. Implementation, usage and validation of this scheme is detailed in the following.

4.2.1 Design of the Interface

Implementation

Referring to the unified modeling language (UML) diagram [17] in Figure4.2, the core of the proposed CAD interface is a mapping between the VCGLIB derived *CADTriMesh* class which is comprised of faces and vertexes, and the GEANT4 *G4 TessellatedSolid* class. This mapping is performed automatically with an instance of the CAD interface *CADMesh* class, and unlike the manual solutions described above, requires no intermediate files or manual manipulations using commercial software. Upon creating an instance of *CADMesh* and supplying it with the file name and type of the target CAD file, an instance of *CADTriMesh* is populated with a mesh described in the CAD file. A VCGLIB import wrapper is used to perform this action, with a *vcg::tri::io:: ImporterPLY* wrapper used to populate *CADTriMesh* with a mesh described in a PLY formatted file for example. At this point, *CADTrimesh* enables access to the contents of the CAD file in a manner that is independent of its format. Other triangular facet mesh importers provided by VCGLIB include: Wavefront geometry definition (OBJ), Geomview object file format(OFF), STL files and more [14].

Given that *CADTriMesh* is now populated with vertexes and faces describing a mesh, the *CADTriMesh::FaceIterator* iterator is used to iteratively instantiate a GEANT4 *G4TriangularFacet* for each face. Subsequently, these faces are added to the tessellated solid using the *G4TessellateSolid::AddFacet* method. Once the iterator has looped over all faces, the *G4TessellatedSolid::SetSolidClosed* method is called, preventing further faces from being added to the volume. The *CADTriMesh* object is set public so the user may interact with it and VCGLIB directly from within GEANT4, however this is not required if the user simply wants to load a supported CAD file into GEANT4.

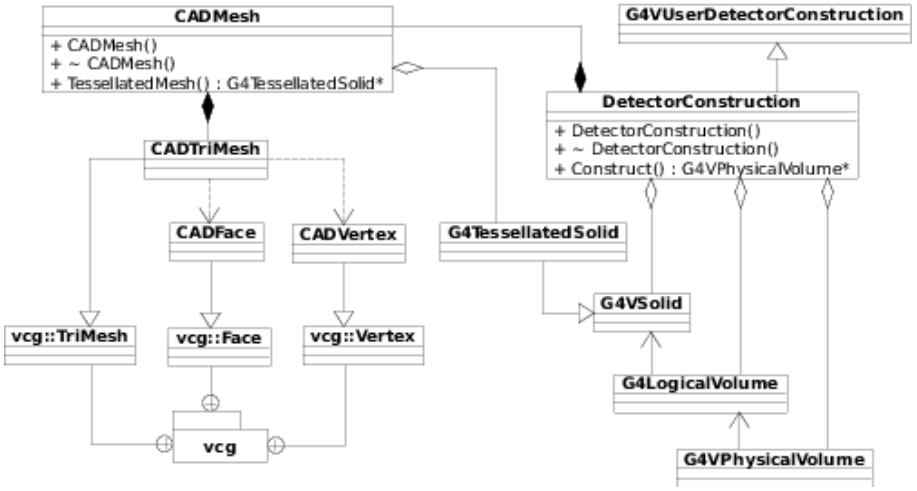

Figure 4.2: UML class diagram showing interaction between VCGLIB, CADMesh and a GEANT4 user detector construction. The symbols have the usual meaning when considering a UML class diagram [17]. C++ class names prefixed by *G4*, *CAD* and *vcg* belong to GEANT4, the described CAD interface, and VCGLIB respectively and *DetectorConstruction* is a user defined class.

Usage

At the user level, all functionality provided by the CAD interface is contained within an instance of the *CADMesh* object, which can be made available to the user with the inclusion of the *CADMesh.hh* C++ header file in the user detector construction. Instantiation of a *CADMesh* object and a call to the *CADMesh:: TessellatedMesh* method generates and returns a *G4TessellatedSolid* suitable for inclusion in the user geometry in the same manner as with any typical *G4VSolid* object. Following the standard GEANT4 geometry hierarchy, material properties and volume meta-data unique to the volume can be assigned with association to a *G4LogicalVolume*, and placement of the *G4TessellatedSolid* within a mother volume with association to a *G4PhysicalVolume*. Constructor arguments include the file name for the file that contains the mesh, a file type identifier, and optional arguments specifying the units of the coordinates described in the file, a *G4ThreeVector* used to offset the mesh in the x, y and z directions, and a boolean option - *reverse*. The reverse boolean option results in faces being added to the *TessellatedSolid* with the order of their vertexes opposite to what is reported in the source CAD file should the vertex order be opposite to what is required for

a *G4TessellatedSolid*. CAD file types currently supported by the interface include OFF, PLY, STL and COLLAborative Design Activity digital asset schema (COLLADA) [18].

The source code of the interface is distributed with an autoconf script for testing for, and locating the required dependencies of the CAD interface, as well as generating a Makefile for compilation of the *CADMesh.so* shared object library. A working installation of GEANT4 is required for successful compilation of the library, additionally the source code for VCGLIB – which is freely available on the internet [14] – is required to enable support for loading OFF, STL and PLY files. From the users perspective however, direct interaction with VCGLIB is not required as it is used internally and automatically by the CAD interface. Once compiled, user code requires linking against *CADMesh.so* in the usual way, a process which is documented as a part of the source code distribution of the library.

4.2.2 Validation of the Interface

Six test volumes were used to verify the performance of the GEANT4 CAD interface. Three simple geometries, a truncated cone and a sphere generated using MeshLab (Visual Computing Laboratory, Italy) and an artificial hip (generated in-house) were saved in all formats capable of import by the CAD interface. Additionally, a flattening filter from a Varian clinical linear accelerator, a single leaf from a Varian multi-leaf collimator and a model of a pelvis from a CIRS Pelvic Phantom (Model 048) were loaded into GEANT4 using the CAD interface. Each volume, when loaded was visually inspected for qualitative geometric integrity using the GEANT4 OpenGL viewer. Tessellated solid meta-data was dumped for each solid using the *G4TessellatedSolid::DumpInfo* method providing a list of each face and vertex coordinate used to define the GEANT4 volume. This data was then compared directly to the original CAD file describing the same

volume. A pass level of 100% matching was set, no rounding errors of the vertex coordinates were accepted and vertex and face counts had to agree exactly.

So as to ensure the loaded geometries were navigable by the GEANT4 kernel, each volume was assigned the material *G4_WATER* and positioned at the center of a *G4_AIR* filled world volume. A general particle source (GPS) was initialized and configured to produce a beam of geantinos (the standard GEANT4 debugging pseudo-particle) aimed at the test volume. Each test volume was bombarded with $100,000$ geantinos with the tracking verbosity level set to one and the step length set to 0.1 mm, ensuring any navigation errors associated with the imported CAD geometry were output; the angular distribution of the beam was set so as to target the entire volume ensuring all faces were inside the beam. At any time, if the navigator was unable to determine if it was inside or outside of the tessellated volume as a consequence of invalid volume definition, the test was failed. Geometry overlap tests build into GEANT4, accessible via the */geometry/test/* user interface commands were also used to verify the correct definition of all geometries loaded using the CAD interface.

4.3 Results

Figure4.3(a), Figure4.3(b) and Figure4.3(c) show three simple geometries loaded into GEANT4 via the CAD interface described in section 4.2.1. Further to this, Figure4.3(d), Figure4.3(e) and Figure4.3(f) show more complex geometries loaded into GEANT4. All test volumes imported using the CAD interface, independent of the CAD file format, passed qualitative visual inspection - no corruption of the geometry was visible. Table 4.1 displays the vertex and face counts for each volume; there was no difference between the vertex and facet counts reported by VCGLIB or GEANT4.

A comparison between the original CAD file and the dumped face and vertex information from each tessellated solid generated no errors. Additionally,

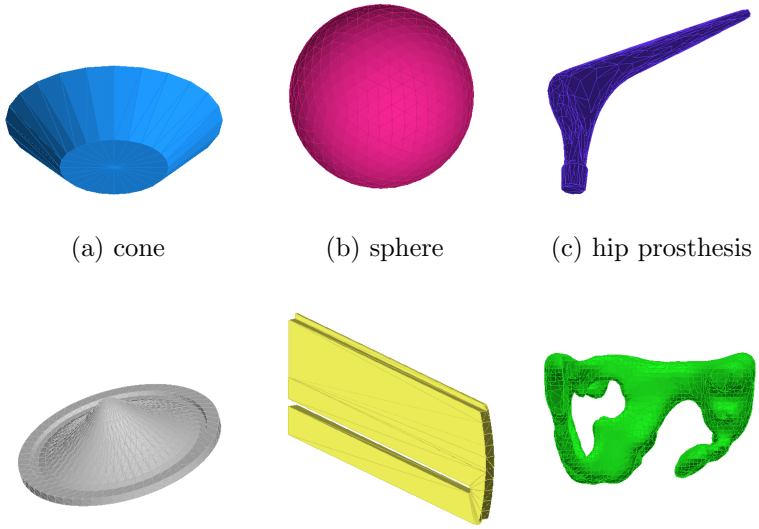

(a) cone (b) sphere (c) hip prosthesis

(d) flattening filter (e) MLC leaf (f) pelvis model

Figure 4.3: Six test geometries loaded directly into GEANT4 using the proposed CAD interface and visualised using the GEANT4 OpenGL viewer.

Name	Verts	Faces	Inspection	Dump/Navigation
cone	50	96	Pass	Pass
sphere	642	1280	Pass	Pass
hip	502	1000	Pass	Pass
leaf	120	236	Pass	Pass
filter	1235	2346	Pass	Pass
pelvis	4986	10000	Pass	Pass

Table 4.1: Properties of the six volume loaded into GEANT4 via the proposed CAD interface.

the inbuilt geometry overlap tests, when performed on all test geometries loaded using the proposed CAD interface, found that the geometry was valid. When bombarded with a simulated source of geantinos, no navigation errors were reported. In the case that a face were to be purposefully excluded from the *G4TessellatedSolid*, the volume would be unnavigable as a consequence of an undefined 'inside' or 'outside', known as a non-closed solid.

The time required to load a mesh using the CAD interface was compared to the time required to load the equivalent geometry from a GDML file. It was found that the load time in both cases was bound by the *G4TessellatedSolid::AddFacet* method. Setup time, including the parsing of the CAD or GDML files was mea-

sured and found to be insignificant compared to the time required to add faces to the *G4TessellatedSolid*.

4.4 Discussion & Conclusion

Using the templated C++ mesh manipulation library VCGLIB, we have demonstrated a technique whereby CAD models may be directly imported as geometry into GEANT4 without the express need for file format conversion using commercial software. Reliability of the interface in terms of preserving model integrity during import was evaluated quantitatively by comparing the vertex coordinates as reported by GEANT4 to the actual vertex coordinates described in the source CAD file. Currently the interface cannot parse material properties or other GEANT4 specific meta-data, the interface is strictly limited to importing geometry or shape information only. A CAD model imported using the interface however, may be saved as part of an assembly in GDML using tools that are already part of the toolkit where its relation to other parts of the detector construction will be preserved.

By removing the intermediate file format conversion step, unnecessary reliance on commercial third party software can be avoided and any CAD model described by a triangular tessellated surface may be directly loaded as a geometry within GEANT4. Fast geometry definition in GEANT4 from CAD models is also useful if the GEANT4 simulation forms part of the experiment design process. Having a CAD geometry for the manufacture of components for example, and a simulation comprised of primitives effectively decouples the simulation from the manufactured part - even if the part is simple. Using a CAD geometry for simulation requires changes (hole positions for example) be made using CAD, which automatically means the manufacture geometry is up-to-date, or perhaps more importantly, the manufacture and simulation geometries are the same.

No navigation errors were reported for any of the test geometries when bom-

barded with a simulated source of geantinos and all tessellated solids in GEANT4 were found to be equivalent to the source CAD geometries. Finally, difference in load time between the method described here, and loading the same geometry using GDML was found to be insignificant as the load time for a tessellated solid in GEANT4 is bound by the time that is required to add each face using the *G4TessellatedSoild::AddFacet* method.

The CAD interface for GEANT4 described in this work is freely available for download on the internet along with installation instructions and usage examples at http://code.google.com/p/cadmesh/

Acknowledgments

This work was supported in part by the Queensland Cancer Physics Collaborative, and Cancer Australia (Department of Health and Ageing) Research Grant 614217.

Bibliography

[1] S. Agostinelli, J. Allison, K. Amako, J. Apostolakis, H. Araujo, P. Arce, M. Asai, D. Axen, S. Banerjee, G. Barrand, et al. Geant4 simulation toolkit. *Nuclear Instruments and Methods in Physics Research-Section A Only*, 506(3):250–303, 2003.

[2] J. Allison, K. Amako, J. Apostolakis, H. Araujo, P.A. Dubois, M. Asai, G. Barrand, R. Capra, S. Chauvie, R. Chytracek, et al. Geant4 developments and applications. *IEEE Trans. Nucl. Sci.*, 53(1):270–278, 2006.

[3] S. Jan, D. Benoit, E. Becheva, T. Carlier, F. Cassol, P. Descourt, T. Frisson, L. Grevillot, L. Guigues, L. Maigne, et al. GATE V6: a major enhancement of the GATE simulation platform enabling modelling of CT and radiotherapy. *Physics in Medicine and Biology*, 56:881–901, 2011.

[4] S. Xiao, X. Yang, M. Sztejnberg, and T. Jevremovic. Geant4 based Monte Carlo dose calculation engine for radiation therapy. *IEEE Trans. Nucl. Sci.*, 57(2):775–781, 2010.

[5] J.F. Carrier, L. Archambault, L. Beaulieu, and R. Roy. Validation of GEANT4, an object-oriented Monte Carlo toolkit, for simulations in medical physics. *Medical Physics*, 31:484–492, 2004.

[6] L. Grevillot, T. Frisson, D. Maneval, N. Zahra, J. N. Badel, and D. Sarrut. Simulation of a 6 MV Elekta Precise Linac photon beam using GATE/GEANT4. *Physics in Medicine and Biology*, 56:903–918, 2011.

[7] M. Constantin, D. E. Constantin, P. J. Keall, A. Narula, M. Svatos, and J. Perl. Linking computer-aided design (CAD) to Geant4-based Monte Carlo simulations for precise implementation of complex treatment head geometries. *Physics in Medicine and Biology*, 55:N211–N220, 2010.

[8] T. Beutier, E. Delage, M. Wouts, O. Serres, and P.F. Peyrard. Fastrad new tool for radiation prediction. In *Proceedings of the 7th European Conference*

on Radiation and Its Effects on Components and Systems, 2003. RADECS 2003., pages 181–183, 2003.

[9] M.J. Pratt. Introduction to ISO 10303 - The STEP standard for product data exchange. *Journal of Computing and Information Science in Engineering*, 1:102–103, 2001.

[10] Initial Graphics Exchange Specification 5. US Product Data Association, 2007.

[11] R. Chytracek, J. McCormick, W. Pokorski, and G. Santin. Geometry description markup language for physics simulation and analysis applications. *IEEE Trans. Nucl. Sci.*, 53(5):2892–2896, 2006.

[12] A. Fabri and S. Pion. CGAL: the Computational Geometry Algorithms Library. In *Proceedings of the 17th ACM SIGSPATIAL International Conference on Advances in Geographic Information Systems*, pages 538–539. ACM, 2009.

[13] S. Rusinkiewicz. Trimesh2: A C++ library and set of utilities for input, output, and basic manipulation of 3D triangle meshes. Computer software. http://www.cs.princeton.edu/gfx/proj/trimesh2, 2011.

[14] A portable C++ templated library for the manipulation, processing of triangle and tetrahedral meshes. Computer software. http://vcg.sourceforge.net/, 2011.

[15] Stereolithography interface specification. 3D Systems Inc, 1989.

[16] PLY - Polygon File Format. Computer software and file format description. http://local.wasp.uwa.edu.au/ pbourke/Dataformats/ply/, 2012.

[17] Unified Modeling Language (UML) Superstructure Specification, v2.3. Object Management Group Inc, 2010.

[18] COLLADA - Digital Asset Schema Release 1.5.0 Specification. The Khronos Group Inc., Sony Computer Entertainment Inc., 2008.

Chapter 5

Fast Tessellated Solid Navigation in GEANT4

Target Journal

IEEE Transactions on Nuclear Science

Publication Status

Accepted for publication, April 2012.

Authors

CM Poole[1,2] *(Candidate)*, I Cornelius[1], JV Trapp[1,†] and CM Langton[1,⋆]

[1] School of Chemistry, Physics and Mechanical Engineering, Science and Engineering Faculty, Queensland University of Technology
[2] Cancer Care Services, Royal Brisbane & Womens Hospital

⋆ Supervisor
† Associate supervisor

Statement of Joint Authorship

CMP conceived the overall concept, developed proof of concept software and wrote the paper. IC assisted in software development and testing. IC, JVT and CML assisted CMP in design, scientific development process and manuscript editing.

This article has been accepted for inclusion in a future issue of this journal. Content is final as presented, with the exception of pagination.

Fast Tessellated Solid Navigation in GEANT4

Christopher M Poole, Iwan Cornelius, Jamie V. Trapp, and Christian M Langton

***Abstract*—Navigation through tessellated solids in GEANT4 can degrade computational performance, especially if the tessellated solid is large and is comprised of many facets. Redefining a tessellated solid as a mesh of tetrahedra is common in other computational techniques such as finite element analysis as computations need only consider local tetrahedrons rather than the tessellated solid as a whole. Here within we describe a technique that allows for automatic tetrahedral meshing of tessellated solids in GEANT4 and the subsequent loading of these meshes as assembly volumes; loading nested tessellated solids and tetrahedral meshes is also examined. As the technique makes the geometry suitable for automatic optimization using smartvoxels, navigation through a simple tessellated volume has been found to be more than two orders of magnitude faster than that through the equivalent tessellated solid. Speed increases of more than two orders of magnitude were also observed for a more complex tessellated solid with voids and concavities. The technique was benchmarked for geometry load time, simulation run time and memory usage. Source code enabling the described functionality in GEANT4 has been made freely available on the Internet.**

***Index Terms*—GEANT4, navigation, tessellated solid, tetrahedron.**

I. Introduction

TESSELLATED solids in Geometry and Tracking (GEANT4) [1], [2] offer a simple method for defining complex and irregular geometry, such as those created using computer aided design (CAD) [3], [4]. Navigation through these tessellated solids however, can be a performance bottleneck, especially if the tessellated solid is defined by many facets and a large number of steps take place within its boundary, see Section III-A. Specifically, the bottle neck occurs when the GEANT4 navigator determines if the current step is inside or outside a tessellated solid.

Every step, at a boundary crossing or forced step governed by the setting of a maximum step length, the GEANT4 navigator determines the current step position relative to the user geometry [1], [2]—if the step is on the surface of a volume, or within a volume for example. For primitives such as cubes, spheres, tetrahedra and others, the determination of position within the volume is $O(1)$, that is to say the computation time required is constant and independent of the size of the volume described by the primitive. Being *primitive* is what gives rise to this property, the volume is well defined and has a specific and expected arrangement of facets. Consider a rectangular prism made up of exactly six faces and eight vertexes, where opposite faces are parallel and adjacent faces are perpendicular. Verifying if an arbitrary point is inside or outside of this prism is a trivial application of minimum and maximum bounds in the x, y, and z directions (assuming of course the prism has not been rotated). For a sphere, a similar operation may be applied, however the bound is applied in the radial direction.

Complex geometries may be too difficult to define with primitives alone; the tessellated solid was introduced to facilitate the definition of CAD derived surface meshes. Results presented in Section III-A show that the time required to navigate a tessellated solid however is $O(n)$, linearly proportional to the number of facets that define the tessellated solid. Inspection of the GEANT4 source code implementing the process of inside determination for a tessellated solid shows that it is a multi-step process requiring iteration over each facet defining the solid. Firstly, a simple bounding box check is performed, if the step is outside of the bounding box, there is certainty the step is not within the tessellated solid and the function exits. Next, each facet is tested and compared to the current step position, if the distance to the facet is within a threshold, the step is considered to be on the volumes surface and the function exits. Finally, if the previous checks fail, 20 random rays are projected from the current step point. Each facet is again iterated over to test if a ray intersects it. The direction of the intersection for the first facet crossed by a ray is determined by examining the normal vector of the facet, for a normal vector of $0 < \theta < \pi/2$ the ray is exiting the solid or if the normal vector is $\pi/2 < \theta < \pi$ the ray is entering the solid. Note that each facet for the tessellated solid must be defined with its vertexes ordered in an anti-clockwise direction such that the normal for the face is pointing to the inside of the solid. This algorithm is described in more detail elsewhere [5], and it is noted that the algorithm is very robust when considering tessellated solids with voids and concavities compared to other techniques which are generally optimised to consider tessellated solids without concavities only.

Geometry optimization techniques already present within GEANT4 such as smart-voxelisation and geometry parameterisation tend not to be effective when applied to tessellated solids. Smart-voxelisation is an automatic partitioning of the geometry where groupings of nearby and smaller volumes are assigned to a common local mother volume, referred to as a smartvoxel [6]. Geometry parameterisation is a technique whereby regular and repeating geometries such as voxelised data can be represented as multiple copies or replicas of the

Manuscript received October 06, 2011; revised February 12, 2012; accepted April 22, 2012. This work was supported in part by the Queensland Cancer Physics Collaborative, and Cancer Australia (Department of Health and Ageing) Research Grant 614217.

C. M. Poole is with Cancer Care Services, Royal Brisbane and Women's Hospital, Herston, QLD 4029, Australia and also with Discipline of Physics, Faculty of Science and Technology, and the Institute of Health and Biomedical Innovation, Queensland University of Technology, Brisbane, QLD 4000, Australia (e-mail: christopher.poole@qut.edu.au).

I. Cornelius, J. V. Trapp, and C. M. Langton are with the Discipline of Physics, Faculty of Science and Technology, and the Institute of Health and Biomedical Innovation, Queensland University of Technology, Brisbane, QLD 4000, Australia (e-mail: iwan.cornelius@qut.edu.au; j.trapp@qut.edu.au; christian.langton@qut.edu.au).

Digital Object Identifier 10.1109/TNS.2012.2197415

0018-9499/$31.00 © 2012 IEEE

This article has been accepted for inclusion in a future issue of this journal. Content is final as presented, with the exception of pagination.

same initial volume. Properties assigned to each copy, such as material and position can be described as a function of copy or replica number without the need to initialise a new volume [7], [8]. As an individual instance of a tessellated solid is not a collection of smaller individual or repeating solids, the navigator cannot take advantage of these optimization techniques. An alternative description of a tessellated solid that made available these techniques for geometry optimization would provide an immediate performance improvement.

Computational techniques such as finite element analysis (FEA) redefine complex closed tessellated surfaces as tetrahedral meshes where each mesh element is a simple tetrahedron [9]. Redefining a tessellated surface in this way allows for computations to be performed considering local tetrahedra only, instead of the entire tessellated volume [9]. As is the case with other computational techniques, navigation through a tetrahedron in GEANT4 is very fast as the geometric properties of the solid are well defined. Herewith we do not attempt to optimise the aforementioned G4TessellatedSolid methods that result in arrested navigation; on the contrary, we offer an alternative geometry definition that allows for discrete tetrahedrons to define the same tessellated solid thereby making available smart-voxelisation for automatic geometry optimization. The technique is evaluated for individual and nested tessellated solids represented as tetrahedral meshes in GEANT4.

II. Methods

A. Tetrahedral Meshing

For ease of integration with GEANT4, the freely available C++ quality tetrahedral meshing generator, TETGEN was chosen for this work The generator may be compiled as a stand-alone application or in this case, as a shared object library for linking with a C++ user application [10]. Many configuration parameters are available to the user when creating a tetrahedral mesh using TETGEN; for example, refinement of pre-existing meshes can be performed, the quality of the generated meshes may be finely controlled and tetrahedron volume constraints may be applied—a comprehensive description of functionality provided by TETGEN is described by others [10]. Using the TETGEN library, two `tetgenio` (the TETGEN input/output object) meshes, `input` and `output`, were initialised. The input mesh was populated with a tessellated triangular facet surface mesh described in a stereo lithography (STL) file using the `tetgenio :: load_stl` method with the mesh file name as an argument. The output mesh was then populated with a constrained Delaunay tetrahedralisation of the input mesh using the TETGEN `tetrahedralize` function with a configuration string and the input and output `tetgenio` objects parsed by reference as arguments. Configuration for the constrained Delaunay tetrahedralisation (enabled with the `p` flag) was such that boundary facet splitting was suppressed (by setting the `Y` flag), thereby preserving the mesh surface described by the input mesh. No mesh quality was specified (ordinarily set with the `q`n flag, where n is an arbitrary value specifying mesh quality), resulting in an output mesh with a minimum of tetrahedra.

Access to individual tetrahedra in the output mesh was available via the `output.tetrahedronlist` vector where every four elements indicated the vertex index numbers of the current tetrahedron. The coordinates of each vertex could then be retrieved from the `out.pointlist` vector. Iterating over the `output.tetrahedronlist` vector, a `G4Tet` solid was initialised along with a `G4LogicalVolume` for each tetrahedron, at which point material properties were also assigned. Subsequently each logical volume was added to a `G4Assembly` Volume allowing for all tetrahedra to be positioned (including translation, rotation and reflection operations) within the user detector geometry as a single entity using the `G4AssemblyVolume :: MakeImprint` class method. Code listing 1 shows example usage for loading the same object described in a CAD file as a tessellated solid or as a tetrahedral mesh using the `cadmesh` CAD interface for GEANT4.

Listing 1: Basic Usage of Tessellated Solid Tetrahedralisation in a User Detector Constructor

```
#include "CADMesh.hh"
…
CADMesh * mesh = new CADMesh("sphere.stl", "STL");


// Tessellated Mesh
G4TessellatedSolid * solid =mesh -> TessellatedMesh();


// OR Tetrahedral Mesh
G4Material * material;
G4AssemblyVolume * assembly =
      mesh -> TetrahedralMesh(material);

// Tetrahedral Mesh Placement
G4Transform3D transform;
assembly -> MakeImprint(mother_logical, transform, 0, 0);

```

B. Simulation Set-Up & Geometry Definition

Using the freely available mesh manipulation program MeshLab [11], a sphere of 400 mm diameter was created with its surface defined by 45,000 tessellated triangular facets. Marching cube mesh refinement in MeshLab was then used to reduce the number of facets defining the sphere in steps of 2,500 to a lower facet count of 2,500, yielding a set of meshes all defining the same sphere over a range of facet counts, see Figs. 1(a) and 1(b) for an example surface mesh with corresponding tetrahedralisation. A more complex mesh, that of a model pelvis (CIRS Multi-modality Pelvic Phantom, model 048) was also created, again using marching cube mesh refinement to create a range of meshes with facet counts between 5,000 and 35,000 facets, see Figs. 1(c) and 1(d).

A simple GEANT4 detector geometry was created with an air-filled (G4_AIR) cube of 1 m edge length initialised as the world volume; the test geometry material was set to water (G4_WATER) and positioned at the center of the world volume.

This article has been accepted for inclusion in a future issue of this journal. Content is final as presented, with the exception of pagination.

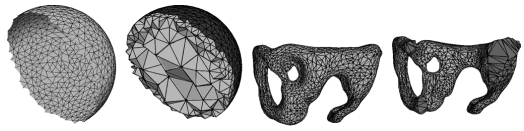

(a) (b) (c) (d)

Fig. 1. Tetrahedral meshing; (a) Shows a cut-away of the triangular tessellated surface of a sphere and (b) Shows its corresponding tetrahedralisation. The tessellated surface of a model pelvis is shown in (c) With its corresponding tetrahedralisation cut-away in (d) (a) Surface mesh (b) Tetrahedral mesh (c) Surface (d) Cut-away.

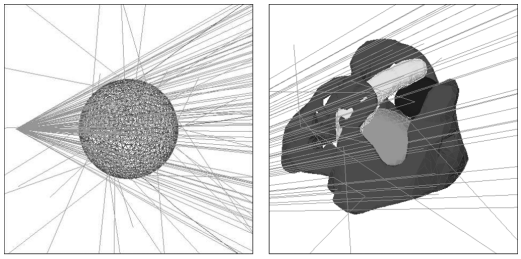

(a) (b)

Fig. 2. The general simulation set-up where the outer box defines the edge of the mother world volume with the test geometry in the center. Test particles are shown fired from the general particle source from left to right in (a).

Standard electromagnetic physics were used throughout by registering the `G4EmStandardPhysics` module in the user physics list; range cuts were set to 1 mm. A general particle source was positioned 5 cm inside the world volume and aimed at the test geometry, see Figs. 2(a) and 2(b); the beam divergence angle was set to 30° thereby ensuring full beam coverage of the test geometry.

C. Computational Performance

Each of the above test geometries were first loaded as native GEANT4 tessellated solids using the `cadmesh` GEANT4 CAD interface, also developed by the authors of the present work [12]. These tessellated solid geometry simulations were used as controls for the equivalent tetrahedral mesh simulations. Smart-voxelisation optimization was automatically disabled by default in GEANT4, as the world mother volume contained only one daughter volume—the `G4TessellatedSolid` test geometry. Subsequently, the test geometries were loaded as tetrahedral meshes using the method described in Section II-A and optimised for a range of smart-voxelisation values between 0.2 and 2.0. For all simulation configurations, the geometry was bombarded with 10^5 `G4Gamma` particles and repeated 10 times; a number of parameters were recorded in order to measure computational performance including; geometry load time, simulation beam on time and smart voxel memory usage. These parameters were then evaluated as a function of source tessellated volume facet count.

D. Geometry Equivalence

Testing was performed so as to ensure the tetrahedral meshes defined the same geometry as the original tessellated solids. Firstly, qualitative visual inspection of the geometry was carried out using the GEANT4 OpenGL viewer, checking that tetrahedral geometry was correctly located within its mother volume. Geometry overlap was tested using the GEANT4/`geometry/test/` user interface commands, ensuring adjacent tetrahedra were in fact adjacent and not overlapping as this could result in navigation error. The maximum extents of the tetrahedral geometry were also calculated and compared to that of the source tessellated solid. Further, the coordinates of all tetrahedra vertices, as loaded in GEANT4, were acquired using the `G4Tet` :: `DumpInfo` class method and compared to the coordinates of the vertices in the source tessellated solid where missing vertices indicated an invalid geometry definition. Finally, a test of missing tetrahedra was devised; the tetrahedral mesh was loaded and geantinos (the GEANT4 debugging pseudo-particle) were fired into the geometry from three orthogonal directions; tracking verbosity was set to one so as to output the unique name of each solid navigated through as the geantinos traversed the user detector geometry. A search through this output was performed so as to verify that all tetrahedra created during the tetrahedralisation of the source tessellated solid were navigable and included in the GEANT4 user detector geometry as `G4Tet` volumes.

E. Nesting Tessellated Solids

For an assembly of nested tessellated volumes it is possible to generate an equivalent tetrahedral mesh using TETGEN, where individual tetrahedra are labelled depending on which nested volume they belong to (by setting the `A` flag in the tetrahedralisation configuration). Regions of interest defining several geometric features found in the CIRS pelvic phantom described in Section II-B, namely the pelvis, prostate, bladder, rectum and body were extracted from a DICOM CT dataset and the constituent vertexes and facets appended to `.node` and `.ele` mesh files respectively. Unique region labels were assigned to each volume thereby ensuring volume boundaries were preserved during tetrahedralisation. Average material properties, calculated statistically from the source CT dataset were assigned to each volume. Iteratively adding the tetrahedra defining the combined mesh as in the same manner described in Section II-A and assigning material properties based on the unique volume label, the equivalent tetrahedral mesh of a collection of nested tessellated volumes was loaded into GEANT4.

The geometric equivalence of the tessellated and tetrahedral geometries was evaluated in the same manner as described previously and computation time and memory consumption was measured for two parallel and opposed 5×5 cm fields aimed towards the prostate from either side of the phantom using a phasespace file from a pre-existing clinical linear accelerator geometry. Using a `G4SensitiveDetector` configured to score radiation dose in both the tessellated and tetrahedral geometries, the dose distribution of the two parallel and opposed fields was calculated and compared using gamma evaluation [13] with a pass/fail criterion of 1 % and 2 mm scored on a 2 mm dose grid. Gamma evaluation is a statistical technique used to quantitatively compare two datasets. The current point in the sample dataset is directly compared to the corresponding point in the reference dataset and points that surround it. Distance penalties

This article has been accepted for inclusion in a future issue of this journal. Content is final as presented, with the exception of pagination.

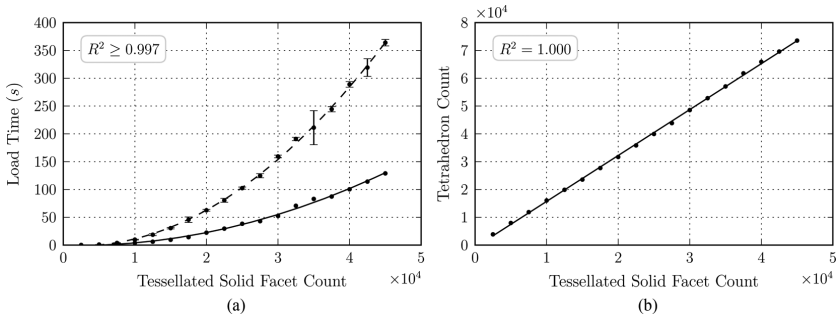

Fig. 3. Geometry load time is shown in (a) Where dashes indicate a second order fit to tetrahedral geometry load time with corresponding measured data and the solid line indicates a second order fit to tessellated geometry load time. Plot (b) Shows tetrahedron count versus tessellated solid facet count with a linear fit.

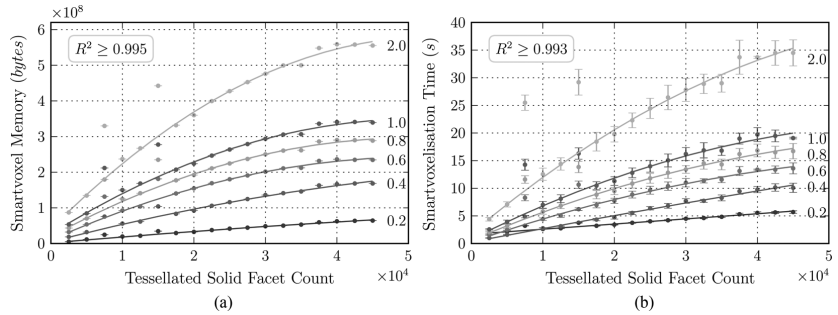

Fig. 4. Smartvoxel memory consumption is shown in (a) Where solid lines indicate a second order fit to the measured data. The time required to perform the smartvoxel geometry optimization is shown in (b) Data labels indicate the smartvoxel value for the dataset.

are applied such that a matching point close to the current point is more heavily weighted compared to one that is further away. The resulting gamma value reports the agreement between the datasets according to the specified pass/fail or distance to agreement criterion with a gamma value $\gamma \leq 1$ indicating a pass and a gamma value $\gamma > 1$ indicating a fail.

III. Results

A. Computational Performance

Fig. 3(a) show the geometry load time for both tessellated and tetrahedral mesh geometries. Specifically, the tessellated geometry load time represents the time required to add all facets to the `G4TessellatedSolid` and position it within the user detector geometry. For the tetrahedral mesh geometry, the load time represents the time required to initialise one `G4Tet` for every tetrahedron in the mesh, add it to a `G4AssemblyVolume` and make an imprint of this same assembly volume in the user detector geometry. Note that the time required to load a tetrahedral mesh as geometry is more than two times that of the time required to load the equivalent tessellated surface mesh; in both cases, load time increases with the square of the number of facets in the source tessellated volume as the operation requires the initialisation of a TETGEN object and a GEANT4 tessellated solid or assembly volume, operations all of which are $O(n)$. Additionally, Fig. 3(b) shows tetrahedron count increasing linearly with increasing source tessellated solid facet count at a rate of 1.60 ± 0.3 tetrahedra per facet. Measured data points in all cases represent the mean value for ten samples and error bars indicate two standard deviations about this mean.

Figs. 4(a) and 4(b) show that the smartvoxel memory consumption increases as a higher smart-voxelisation parameter is specified, as does the time required to perform the voxelisation. Further, as the facet count of the source tessellated solid increases, hence an increasing tetrahedron count, again the smartvoxel memory consumption increases along with the time required to perform the smart-voxelisation. Smart voxel memory consumption was found to be proportional to the smartvoxel count with smartvoxel memory consumption and smart-voxelisation time both proportional to the square root of tessellated solid facet count. Data points at 7,500 and 15,000 facets were excluded from analysis due to the exceptionally large number of smart voxels generated during the optimization of these geometries; these artefacts are examined later.

For increasing facet count, Figs. 5(a) and 5(b) show that simulation run time increases linearly with $R^2 \geq 0.95$ for both a tessellated solid and its equivalent tetrahedral geometry as a function of source tessellated solid facet count. Spheres described as a tessellated solid with more than 10,000 facets showed speed-ups of more than two orders of magnitude. As with previous analysis, data points at 7,500 and 15,000 facets were excluded.

This article has been accepted for inclusion in a future issue of this journal. Content is final as presented, with the exception of pagination.

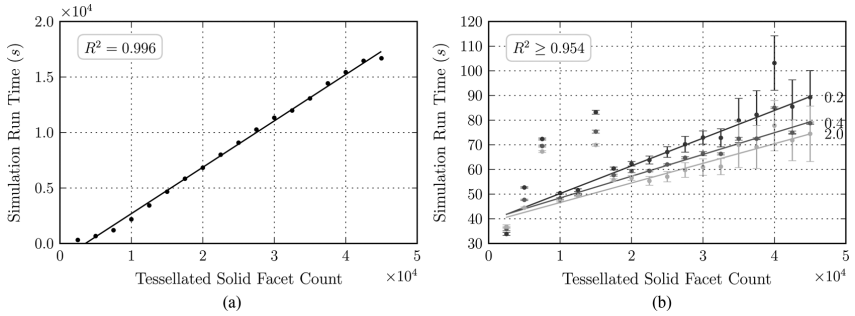

Fig. 5. Simulation run time for 100,000 initial histories and a tessellated geometry is shown in (a), and (b) Shows the simulation time for the equivalent tetrahedral geometry for selected smart-voxelisation value (others omitted for clarity). Data labels in (b) Indicate the smartvoxel value used.

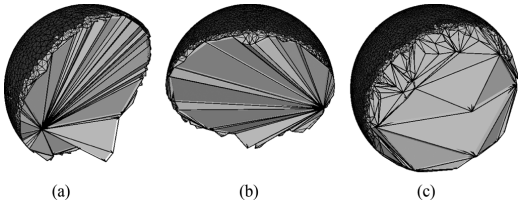

Fig. 6. Meshing artefacts in (a) and (b) That result in suboptimal smart-voxelisation compared to a typical tetrahedralisation in (c). (a) 7,500 facets (b) 15,000 facets (c) 17,500 facets.

Figs. 4(a), 4(b) and 5(b) display artefacts due to higher numbers of smartvoxels generated at 7,500 and 15,000 facets when compared to the underlying trend, noting that the number of tetrahedral generated for these meshes follows the expected linear trend in Fig. 3(b). Inspection of the these tetrahedral meshes in Figs. 6(a) and 6(b) show a characteristic tetrahedron arrangement; specifically the majority of tetrahedra all share a common vertex, this is particularly evident when compared to the typical tetrahedron arrangement shown in Fig. 6(c) for a source tessellated solid of 17,500 facets.

B. Complex Geometry

For the complex mesh geometry show in Figs. 1(c) and 1(d) the tetrahedra generated per facet in the source tessellated solid was found to be 1.77 ± 0.05 tetrahedra per facet, higher than that found for the spherical test geometry. Tetrahedral geometry load time was again found be to more than twice that of the native `G4TessellatedSolid` load time. Simulation time for the tetrahedral geometry was over two orders of magnitude faster than the equivalent tessellated solid geometry for meshes with over 20,000 facets. As with the spherical geometry, smartvoxel memory usage increased with increasing facet count and smart-voxelisation value.

C. Geometry Equivalence

All tetrahedral meshes were found to be geometrically equivalent in GEANT4 to the source tessellated mesh from which they were derived. Using the inbuilt geometry overlap testing in GEANT4, no overlapping tetrahedra were found in any geometry configuration. Direct comparison of the tetrahedra vertex coordinates to the coordinates of the facet vertexes in the source tessellated meshes showed no difference in the boundary definition of the meshes. Further, firing geantinos into the test geometry from three orthogonal directions showed that all tetrahedra defined in the tetrahedralisation of the source tessellated mesh were correctly loaded as native `G4Tet` tetrahedrons in GEANT4.

D. Nesting Tessellated Solids

Figs. 7(a)–7(b), show the progression of nested surfaces to a nested tetrahedral mesh. Using the same methods as described previously, it was found that the volume boundaries defining the surface models were exactly reproduced in the tetrahedral mesh. Isodose contours are shown in Fig. 8(a) for the tessellated geometry representation of the CIRS pelvic phantom. Using gamma evaluation, the comparison between these dose distributions is shown in Fig. 8(b). For a 2 mm dose scoring grid and a pass fail criterion of 1% and 2 mm, 100% of all points within the phantom pass the gamma evaluation when comparing the tessellated and tetrahedral geometries. That is to say no voxel in one grid when compared to the corresponding voxel in the other grid had a dose that was different by greater than 1%. The tetrahedral geometry representation required one fifth the simulation time required for the equivalent tessellated geometry.

IV. Discussion & Conclusion

We have demonstrated fast navigation of tessellated volumes using tetrahedral meshes as an alternative to native `G4TessellatedSolid's` in GEANT4. Using the C++ library TETGEN, automatic tetrahedral meshing of the input tessellated solid can be performed and the resultant tetrahedral mesh placed within the user geometry as an assembly volume. For simple tessellated solids with more than 10,000 facets, navigation has been found to be over two orders of magnitude faster when the solid is loaded as a tetrahedral mesh. Navigation through the complex pelvis tessellated solids, with more than 20,000 facets was also found to be over two orders of magnitude faster when loaded as a tetrahedral mesh. Speedup when considering nested geometries is diminished due to a higher tetrahedron to tessellated facet ratio, however there is

This article has been accepted for inclusion in a future issue of this journal. Content is final as presented, with the exception of pagination.

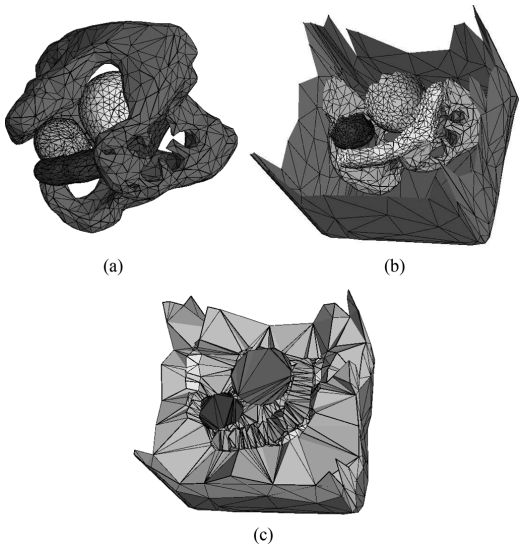

Fig. 7. For the nested tessellated solids in (a) For a phantom pelvis (medium gray), bladder (light gray), rectum (dark gray) and prostate (gray), the equivalent tetrahedral mesh is shown in (b) A cut-away for all source tessellated solids including the mother body volume is shown in (c) Colors are arbitrary and simply indicate separate solids.

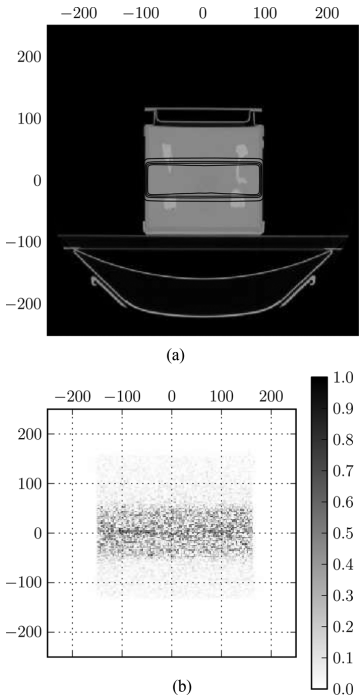

Fig. 8. Isodose contours for the tessellated geometry are shown in (a) with the contours representing 20, 60, 80, 95% of the mean dose at the iso-centre. The gamma evaluation comparing the tessellated and tetrahedral geometries in shown in (b) with a pass fail criterion of 1% and 2 mm.

still a significant speedup when using the tetrahedral equivalent geometry compared to the source tessellated geometry. Whilst the load time for a tetrahedral mesh can be over twice the load time for the equivalent tessellated solid, this can be considered insignificant when the load time may be on the order of minutes, and simulation time on the order of hours, as is the case in this study.

Low quality tetrahedral meshes where many tetrahedra share a common vertex may result in sub-optimal smart-voxelisation. Using TETGEN, higher quality meshes may be generated in order to avoid this vertex sharing artefact, however quality meshing will result in more tetrahedra being created, which in turn will result in higher smartvoxel memory consumption. Specific tetrahedra arrangement is very much dependant on the volume defined by the source tessellated solid, though limited user supervision should be sufficient to capture poor quality meshing and evaluate its significance on the performance of a simulation.

Memory consumption for geometries exploiting smart-voxelisation must be closely managed, especially if the user geometry contains many volumes, as is the case for tetrahedral meshes which may contain tens of thousands of tetrahedra. Tuning the degree of smart-voxelisation allows for basic control of geometry memory consumption and simulation run time. Evaluating the results shown in Figs. 4(a) and 4(b) however, shows that increasing the aggressiveness of the smartvoxel optimization results in small simulation time reductions whilst increasing memory usage from tens of megabytes to hundreds of megabytes. This increase in memory usage may result in suboptimal computation performance in an environment where multiple simulation instances are running on the same computer and all of the available memory is consumed by the simulation. In this case, reducing the smart-voxelisation parameter will reduce memory consumption substantially whist effecting only a small increase on simulation run time.

By remeshing tessellated solids as tetrahedral meshes, smart-voxelisation is made available for geometry optimization. This allows for the GEANT4 navigator to consider only local tetrahedra rather than the tessellated solid as a whole at each step. Consequently, the computationally intensive inside determination for tessellated solids need not be performed during navigation. Using this technique, a significant reduction in simulation run time is observed for user geometry containing tessellated solids defined by many facets.

REFERENCES

[1] S. Agostinelli *et al.*, "Geant4 simulation toolkit," *Nuclear Instrum. Methods in Phys. Res.-Section A Only*, vol. 506, no. 3, pp. 250–303, 2003.

[2] J. Allison *et al.*, "Geant4 developments and applications," *IEEE Trans. Nucl. Sci.*, vol. 53, no. 1, pp. 270–278, 2006.

[3] M. Constantin, D. E. Constantin, P. J. Keall, A. Narula, M. Svatos, and J. Perl, "Linking computer-aided design (CAD) to Geant4-based monte carlo simulations for precise implementation of complex treatment head geometries," *Phys. Med. Biol.*, vol. 55, pp. N211–N211, 2010.

This article has been accepted for inclusion in a future issue of this journal. Content is final as presented, with the exception of pagination.

[4] R. Chytracek, J. McCormick, W. Pokorski, and G. Santin, "Geometry description markup language for physics simulation and analysis applications," *IEEE Trans. Nucl. Sci.*, vol. 53, no. 5, pp. 2892–2896, Oct. 2006.

[5] P. Schneider and D. Eberly, *Geometric Tools for Computer Graphics*. Waltham, MA: Morgan Kaufmann, 2003.

[6] G. Cosmo, "The geant4 geometry modeler," in *Proc. IEEE Nucl. Sci. Symp. Conf. Rec.*, 2004, vol. 4, pp. 2196–2198.

[7] T. Aso, A. Kimura, T. Yamashita, and T. Sasaki, "Optimization of patient geometry based on ct data in geant4 for medical application," in *Proc. IEEE Nucl. Sci. Symp. Conf. Rec. (NSS)*, 2007, vol. 4, pp. 2576–2580.

[8] P. Arce, J. Apostolakis, and G. Cosmo, "A technique for optimised navigation in regular geometries," in *Proc. IEEE Nucl. Sci. Symp. Conf. Rec. (NSS)*, pp. 857–859.

[9] O. Zienkiewicz and R. Taylor, *The Finite Element Method For Solid and Structural Mechanics*. Oxford, U.K.: Butterworth-Heinemann, 2005, vol. 2.

[10] "Tetgen: A quality tetrahedral mesh generator and a 3D delaunay triangulator," Computer Software, Apr. 1, 2012. [Online]. Available: http://tetgen.berlios.de/

[11] "MeshLab: An open source, portable, and extensible system for the processing and editing of unstructured 3D triangular meshes," Computer Software, Apr. 1, 2012. [Online]. Available: http://meshlab.sourceforge.net/,

[12] "CADMESH: A CAD Interface for GEANT4," Computer Software, Apr. 1, 2012. [Online]. Available: http://code.google.com/p/cadmesh/

[13] M. Wendling, L. Zijp, L. McDermott, E. Smit, J. Sonke, B. Mijnheer, and M. van Herk, "A fast algorithm for gamma evaluation in 3D," *Med. Phys.*, vol. 34, p. 1647, 2007.

Chapter 6

Three-dimensional Patient Contours as Geometry for Monte Carlo Simulation

Target Journal

Medical Physics

Publication Status

To be submitted soon.

Authors

CM Poole[1,2] *(Candidate)*, I Cornelius[1], JV Trapp[1,†] and CM Langton[1,⋆]

[1] School of Chemistry, Physics and Mechanical Engineering, Science and Engineering Faculty, Queensland University of Technology
[2] Cancer Care Services, Royal Brisbane & Womens Hospital

⋆ Supervisor
† Associate supervisor

Statement of Joint Authorship

CMP conceived the overall concept, developed proof of concept software and wrote the paper. IC assisted in software development and testing. IC, JVT and CML assisted CMP in design, scientific development process and manuscript editing.

Abstract

Purpose: Using voxelised CT datasets as patient geometry within a Monte Carlo simulation can present a memory and computation overhead. Here we present a technique where the patient geometry may be defined alternatively using regions of interest found in a standard DICOM-RT treatment plan, thereby reducing this overhead. Additionally we show how the technique can be used to augment otherwise static CT data with motion information.

Methods: Contours were extracted from the DICOM-RT treatment plans of a 6-field prostate patient plan and meshed, forming a collection of tessellating tetrahedra. Material properties were assigned to the meshed contours based on average material properties found in the equivalent part of the CT dataset. Monte Carlo simulations were performed using the source voxelized CT data set, and the alternative meshed contour geometry. Dosimetric equivalence was then statistically evaluated using gamma evaluation, and computational performance determined using measured computation time. This process was repeated on a 2-field pelvic phantom treatment plan, with a range of sinusoidal motions assigned to a volume.

Results: For a simulation that uses only the meshed surface of the skin, and compared to the simulation of the full CT dataset, at 4%, 4 mm, 96% of points have a gamma index less than 1.0, and at 2%, 2 mm, 85% of points have a gamma index less than 1.0. The body only simulation produced this results in 5% of the time required to simulate the equivalent voxelised CT dataset.

Conclusions: Using the technique can reduce the computational overhead of Monte Carlo simulations of patient geometry, providing a result in less than one twentieth the time compared to using vox-

elised CT data for relatively homogeneous geometries. Additionally we show that the technique has possible uses in the augmentation of otherwise static CT datasets with motion information.

6.1 Introduction

Monte Carlo simulation applied to radiotherapy has its own unique challenges when compared to other radiation transport problems, especially when considering the definition of the patient anatomy within the simulation geometry. Usually treatment planning DICOM-RT CT data sets are used to define this patient geometry as it offers a high resolution description of the anatomy at the time of treatment planning. Additionally, tissue types and bulk material properties can be determined from the CT numbers represented in the data-set as voxel intensity. However, these CT datasets can present a significant computational memory overhead due to their large size, especially in GEANT4. Increasingly, GEANT4 [1, 2] is being used as a tool for Monte Carlo simulation of clinical linear accelerators and the verification of radiotherapy patient treatment plans [3–5]. EGSnrc with its accompanying user codes BEAMnrc and DOSXYZnrc have long been popular for this same purpose, however GEANT4 offers more flexible geometry and detector definition including time dependant geometries and geometries derived from computer aided design (CAD) models [6, 7].

A number of studies have examined the performance of GEANT4 Monte Carlo simulations with voxelised CT data set geometries [8–13]. Numerous techniques for describing a voxelised geometry are available to the user in GEANT4, ranging from memory inefficient models where each voxel is its own `G4Box` with unique meta-data, to more memory efficient models such as parameterised volumes [13], where many voxels are replicas of a single template volume. During simulation the of a parameterised geometry, the navigator can determine the properties of the current voxel based on its copy number relating it to the original template volume. For the assignment of material properties, a conversion ramp is used whereby ranges of CT numbers are grouped and correlated with particular materials and densities [14, 15]; with this technique, the patient geometry is in-effect segmented by automatic thresholding.

Analytical solutions have also been explored as a means of defining a patient-like anatomy within a Monte Carlo simulation without the express need for voxelisation [16–20]. Indeed Guatelli *et at* show that analytical patient geometries can be very fast to navigate and very easy to define [16]; such solutions allow for faster boundary crossing detection and inside/outside of volume determination. Peter *et at* make direct comparison between analytical and equivalent discrete CT data representations applied to nuclear medicine Monte Carlo simulation [17]. It was shown that a analytical geometry description was sufficient to accurately describe the geometry when compared to the CT dataset, whilst significantly reducing memory consumption and computation time. Sarrut *et at* showed that significant computation performance increases could be achieved in GEANT4 when redefining a CT dataset as a collection of larger homogeneous regions grouped by material – this simplification required the introduction of a new solid in GEANT4 [18]. Furthermore, the possibility of motion augmentation has been discussed by others when considering alternative definitions of patient anatomy compared to that of a CT dataset [19]. Zhu *et al* suggest an entire anatomical geometry defined as a collection of individual volumes that are not discrete as in a CT dataset allow for complex Monte Carlo simulations including motion and deformation [20].

Radiotherapy treatment planning requires the delineation or manual segmentation of the target as well as surrounding anatomical structures. These regions of interest (ROI) or contours are stored as in the DICOM-RT treatment plan for every slice [21]. By meshing the ROIs described in a DICOM-RT treatment plan we propose a method that aims to redefine a patient geometry suitable for use in GEANT4 as an alternative to using a voxelised x-ray CT dataset. We examine the simulation efficiency and accuracy of this technique when compared to a conventional and memory efficient voxel based geometry definition using nested parameterised volumes [13]. Additionally, we show that a geometry defined in this way can be augmented with motion information for the purposes of time

dependant dose calculation [22–24] following that proposed by others [20].

6.2 Materials & Methods

6.2.1 Monte Carlo simulation

Using specifications provided by the manufacturer, a complete CAD model of the beam line of a Varian clinical linear accelerator was created, including both geometry and material composition information from the electron target to the treatment head exit window, including the multi-leaf collimator (MLC) bank. This CAD model was then loaded as geometry in GEANT4 using a technique described by the authors elsewhere [7]. A process of commissioning the Monte Carlo model was undertaken so as to match beam profiles, depth doses and output factors for a number of square fields to quality assurance measurements made with the linear accelerator.

6.2.2 Reference Voxel Geometry

A 6-field 3D conformal prostate treatment plan was created using Varian Eclipse. The voxelised CT data from the treatment plan was then loaded as geometry in GEANT4 using the nested parameterised volumes technique described by Aso [13]. Once loaded, Hounsfield unit CT numbers were converted to a material with a specific atomic composition and density using conversion ramps [14, 15]. Each of the fields in the treatment plan were then simulated using Monte Carlo where dose deposited was scored using the method described in section 6.2.4. This voxel CT based simulation served as the reference for the evaluation of the ROI based simulations described below.

6.2.3 Alternative ROI Geometry

DICOM-RT stores patient contours, as defined by the clinician using a treatment planning system, as part of its standard [21]. Using the Python DICOM toolkit, `pydicom`, the individual contours for each region of interest contained within the prostate treatment plan were extracted. Each contour is defined in DICOM-RT as a list of x, y and z coordinates on the surface of the contour in the CT scanner coordinate system. This 3D point cloud for each region of interest was saved and used as the vertex input into a Poisson surface meshing algorithm available in the MeshLab (Visual Computing Laboratory, Italy) mesh manipulation computer software. Poisson surface meshing is a technique where the entire point cloud is considered when formulating the series of interconnects between points that form the final mesh and is described in detail by others [25]. The final mesh was then saved in the plain-text Stanford Triangle Format (PLY) file format.

Using the CADMesh CAD interface [7, 26] for GEANT4, each region of interest was loaded into GEANT4 within a `G4Box` mother volume with its center positioned at the linear accelerator iso-center. Material properties were assigned according to the mean CT number for the region of interest, which was calculated by masking the voxel CT dataset with each meshed ROI. To transform the ROI meshes into the linear accelerator coordinate system, the x, y and z coordinate for the iso-center described in the CT scanner coordinate system, was subtracted from each mesh vertex coordinate. A single rotation of the mother `G4Box` by 90° about the x axis in the linear accelerator coordinate system completed the transformation.

Simulations of the meshed ROI geometry were then performed in 2 modes. The first used each ROI surface mesh as the geometry, represented as a tessellated solid in GEANT4. Previous work by the authors has shown that this tessellated solid representation in GEANT4 can be suboptimal, and navigation through such a geometry can be accelerated by remeshing tessellated surface geometries as

tetrahedral meshes [26] Accordingly, the second mode of simulation used this tetrahedral representation. This tetrahedral representation was itself performed for 2 different configurations, first the body only or the patient outline was used, and the second with the body including the femoral heads, the rectum, bladder and prostate regions of interest. The tessellated and tetrahedral representations where then compared to the reference voxel CT dataset dose calculation using gamma evaluation [27, 28].

6.2.4 Dose Scoring

In GEANT4 Logical volumes within the simulation geometry can be used as dose detectors. For tessellated solids, each region of interest defined can be set as a separate detector, and for the voxelised geometry the whole dataset can be set as a detector only. The class `DoseDetector`, inheriting from `G4VSensitiveDetector` was defined taking a detector name and histogram resolution as initialisation parameters along with two 3D data arrays for dose and error scoring. Every hit or energy deposit event, the `DoseDetector::ProcessHits` method was called with a `G4Step` as an argument. From the `G4Step` argument, the position of the current event, energy deposit and density of the voxel at the current position was determined. Using this information a voxel in the dose and error histograms was incremented with energy per unit mass and the square of this dose respectively. Dose per primary particle using the values stored in the dose and error vector arrays was calculated using a method described by others [29].

6.2.5 Augmenting with Motion Information

The voxelised CT data of a pelvic phantom (CIRS 048) was processed and loaded as geometry in the same manner as described above. A total of five contours were extracted including the body, pelvis, bladder, rectum and prostate using a method described by the authors in previous work with the same phantom [26].

Taking advantage of the time-dependant geometry functionality within GEANT4, sinusoidal motion was assigned to the prostate perpendicular to 2 conformal and opposed fields in the z direction. Time dependant geometry in GEANT4 allows the user to update translations and rotation of objects on a per-event basis, that is to say every time a new particle is produced in the source, or every time a particle steps in the geometry. The rate of stepping and the frequency of the updating is fully controllable by the user, in this case, every 1,000 primary particles, the geometry was incremented by 1 s worth of motion. Again, gamma evaluation was used to compared the dose distributions for a range of sinusoidal motions in the z direction to that of a static target volume.

6.3 Results

Figure 6.1 shows the extracted regions of interest from the prostate treatment plan DICOM structure set and meshed using the method described in section 6.2.3. The regions of interest do not describe the entire patient anatomy and are strictly limited to describing important features around the treatment site as delineated in the clinic. For the prostate plan, the left and right femoral heads were assigned the average CT values of 1236 ± 1 and 1212 ± 1 respectively, corresponding to cortical bone as calculated from the source CT dataset. The bladder, rectum and prostate were assigned CT values of 1018 ± 1, 1042 ± 1 and 1051 ± 1 corresponding to soft tissue. For the body, the average CT value was calculated to be 1087 ± 1, also corresponding to soft tissue. The region surrounding the body was set to air with a density of 0.044 g/cm^3.

Once tetrahedral meshing of the regions of interest was performed, the result of which is shown in figure 6.2, the complete geometry was loaded into GEANT4. Note that the region boundaries in the tetrahedral mesh exactly conformed the source tessellated mesh boundaries. Simulation results of the 6 field prostate treatment plan are shown in figure 6.3; specifically results of the raw CT dataset,

body only and all regions of interest geometries are shown. Gamma evaluation was used to directly compare these results, figures 6.4, 6.5 and 6.6 show the results of the evaluation comparing the CT and body, CT and ROI, and body and ROI simulations for distance to agreement criterion of 4%, 4 mm and 2%, 2 mm.

For the gamma evaluation comparing the full CT dataset to the body only simulation, at 4%, 4 mm, 96% of points have a gamma index less than 1.0, and at 2%, 2 mm, 85% of points have a gamma index less than 1.0; for the full CT dataset compared to the simulation containing all regions of interest, again 96% and 85% of points have a gamma index less than 1.0. When comparing the two region of interest based geometries, 99% and 98% of points have a gamma index less than 1.0 for 4%, 4 mm and 2%, 2 mm respectively. Most of the points that fail the gamma evaluation with a gamma index greater than 1, occur around the outer edge of the patient surface, where the meshed region of interest does not exactly conform to the raw CT dataset. Total compute time relative to the source CT dataset was found to be 43.5%, 20.4% and 5.1% for the tessellated regions of interest, tetrahedral regions of interest and the tetrahedral body only representation. These relative measures of time include all parts of the simulation including generation of phase space files at the exit window and subsequent simulation of the alternative geometries.

For a range of motion amplitudes dose volume histograms normalised to the mean volume dose in the z direction is shown in figure 6.7 for the meshed phantom geometry. With increasing amplitude, the dose coverage to the prostate decreases when the motion is perpendicular to the beams, as is the case in 6.7.

6.4 Discussion & Conclusion

Here within we describe a technique whereby regions of interest found within DICOM-RT radiotherapy treatment plans may be loaded as geometry in a Monte Carlo simulation as an alternative to raw CT datasets. Gamma evaluation has

been used to compare the dose distributions generated using the technique when compared to the results produced when using the equivalent CT dataset as geometry. Given that the technique describes the patient geometry as a number of separate anatomical volumes, time dependant geometry functionality within GEANT4 may be exploited to calculate the dose to moving patient targets. In this case we have demonstrated a proof of concept whereby a static CT dataset may be augmented with 4D data for this purpose. Furthermore, we suggest that the technique may be valuable in rescuing corrupted CT data-sets for example, or including metallic prosthesis in a simulation geometry; this potential is illustrated in figure 6.8.

Using gamma evaluation to compare varying configurations of the same patient geometry, we show that just the outer surface of the patient anatomy, loaded as a mesh within the simulation geometry is sufficient to calculate a dose distribution that is similar to result produced if the raw CT dataset is used as geometry. Whilst there is a measurable difference between a dose distribution produced using the raw CT dataset and a geometry described using the technique presented here within, the 20 times speedup in simulation time presents a rapid way of acquiring a Monte Carlo based dose distribution for a given treatment plan.

In addition to the reduction in computation time required to obtain a dose distribution, the technique has a wide range of applications when considering the inclusion of foreign bodies within the patient geometry such as metallic implants and radiation sources.

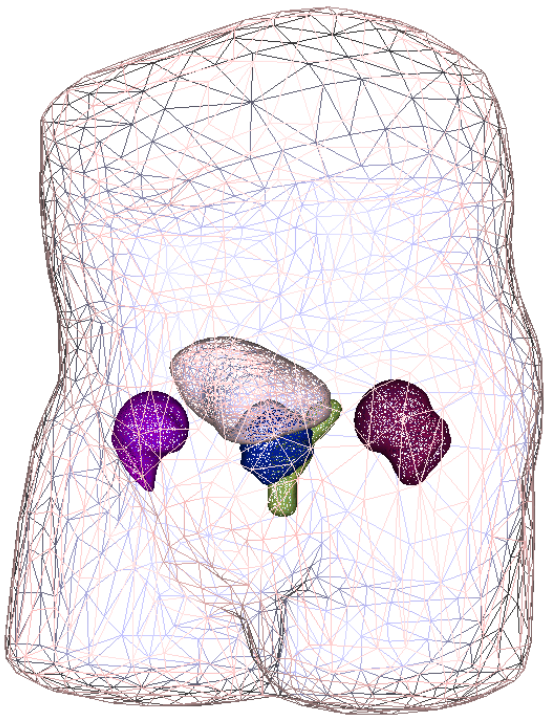

Figure 6.1: Poisson meshes of the regions on interest contained with the DICOM-RT treatment plan.

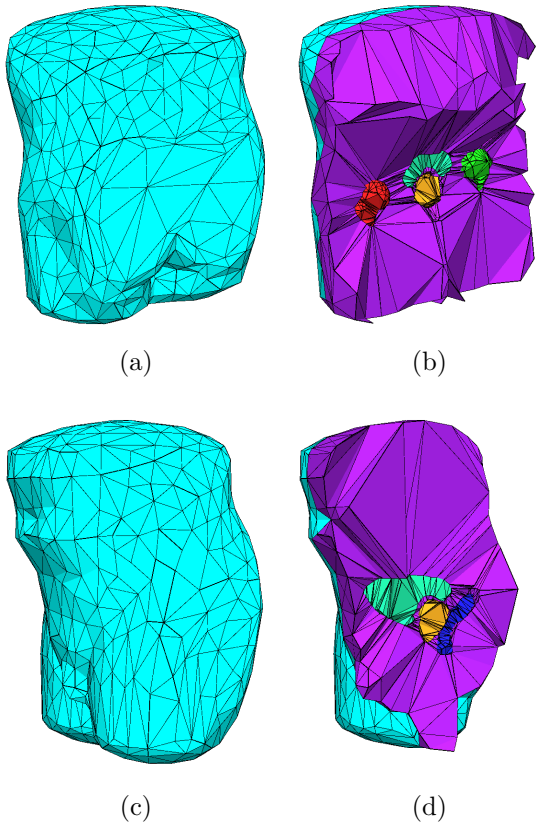

Figure 6.2: Tetrahedral meshing of the regions of interest found in a DICOM-RT radiotherapy treatment plan; (b) and (d) show sections detailing the tetrahedral meshes of the internal regions of iterest with (a) and (c) showing reference orientations. In (b), left (red) and right (green) femoral heads, prostate (yellow), and bladder (cyan), the rectum (dark blue) is shown in (d).

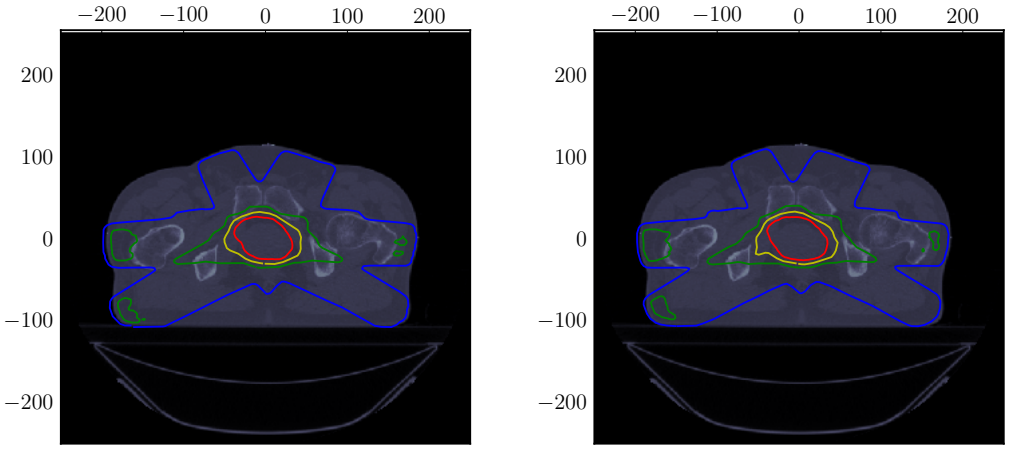

(a)

(b)

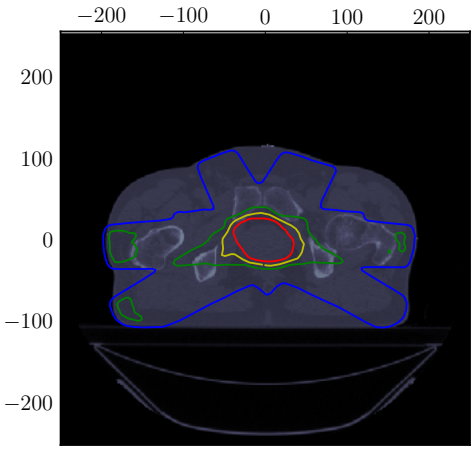

(c)

Figure 6.3: Dose distributions at levels 20 (blue), 60 (green), 80 (yellow) and 100% (red) relative to the mean dose to the target volume are shown for the full CT dataset simulation in (a), the body region only in (b) and all available regions in interest in (c)

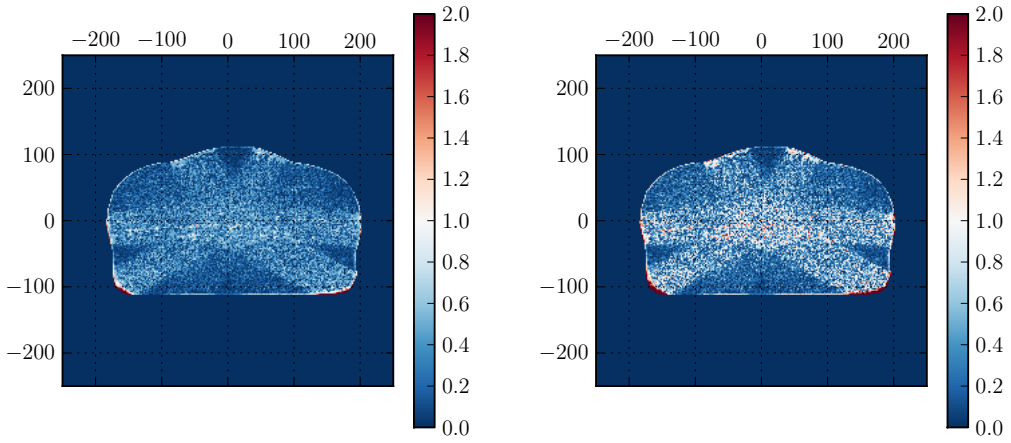

(a) (b)

Figure 6.4: Gamma evaluation comparing the CT dataset simulation to the body only region of interest for a distance to agreement criterion of 4%, 4 *mm* in (a) and 2%, 2 *mm* in (b)

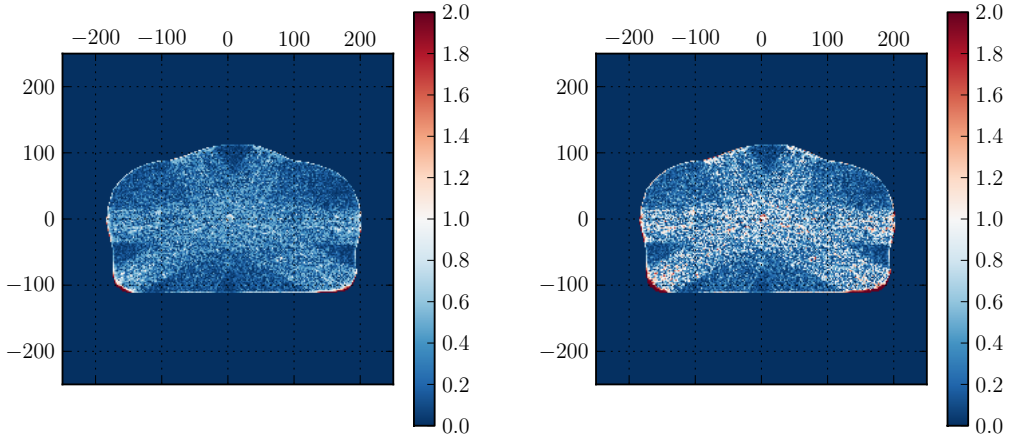

(a) (b)

Figure 6.5: Gamma evaluation comparing the full CT dataset simulation to all regions of interest for a distance to agreement criterion of 4%, 4 *mm* in (a) and 2%, 2 *mm* in (b)

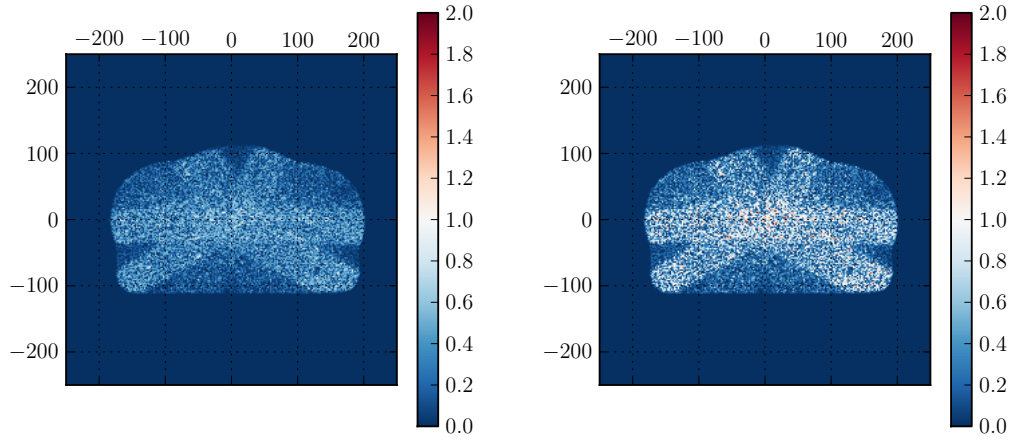

(a) (b)

Figure 6.6: Gamma evaluation comparing the body only region of interest to all regions of interest for a distance to agreement criterion of 4%, 4 *mm* in (a) and 2%, 2 *mm* in (b)

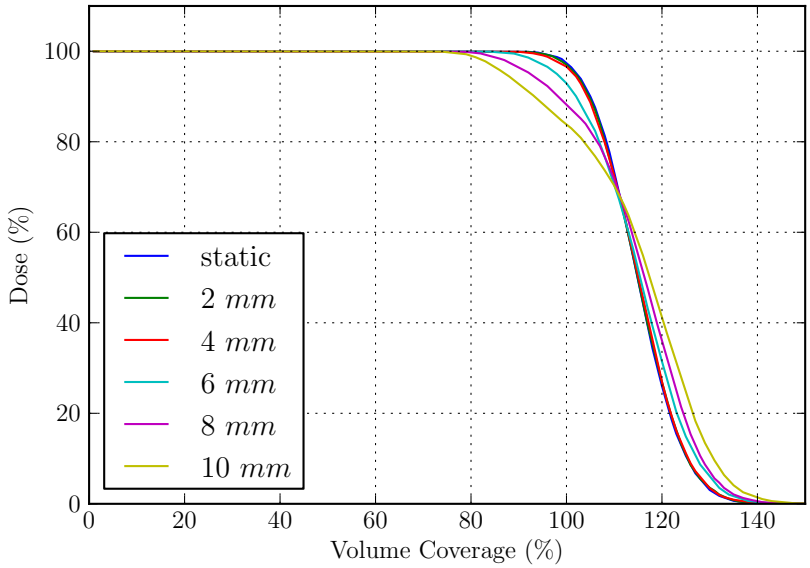

Figure 6.7: Dose volume histogram (z-direction) for a range of amplitudes as indicated.

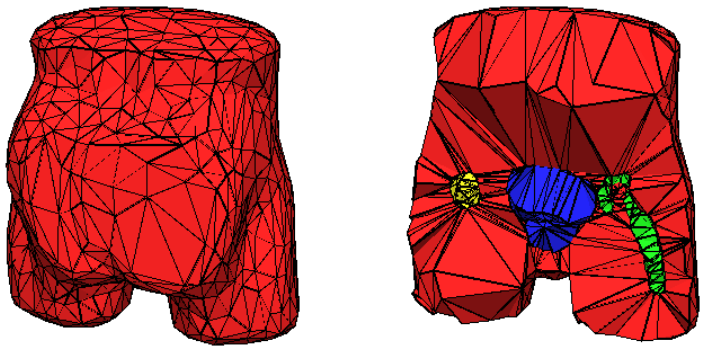

(a) (b)

Figure 6.8: In (a) the orientation of the geometry is shown, (b) shows a cut-away of the tetrahedral geometry showing the inclusion of a metalic implant.

Bibliography

[1] J. Allison, K. Amako, J. Apostolakis, H. Araujo, P.A. Dubois, M. Asai, G. Barrand, R. Capra, S. Chauvie, R. Chytracek, et al. Geant4 developments and applications. *IEEE Trans. Nucl. Sci.*, 53(1):270–278, 2006.

[2] S. Agostinelli, J. Allison, K. Amako, J. Apostolakis, H. Araujo, P. Arce, M. Asai, D. Axen, S. Banerjee, G. Barrand, et al. Geant4 simulation toolkit. *Nuclear Instruments and Methods in Physics Research-Section A Only*, 506(3):250–303, 2003.

[3] S. Jan, D. Benoit, E. Becheva, T. Carlier, F. Cassol, P. Descourt, T. Frisson, L. Grevillot, L. Guigues, L. Maigne, et al. GATE V6: a major enhancement of the GATE simulation platform enabling modelling of CT and radiotherapy. *Physics in Medicine and Biology*, 56:881, 2011.

[4] B. Caccia, C. Andenna, and G. A. P. Cirrone. MedLinac2: a GEANT4 based software package for radiotherapy. *Annali dell'Istituto superiore di sanità*, 46:173–177, 2010.

[5] L. Grevillot, T. Frisson, D. Maneval, N. Zahra, J. N. Badel, and D. Sarrut. Simulation of a 6 MV Elekta Precise Linac photon beam using GATE/GEANT4. *Physics in Medicine and Biology*, 56:903, 2011.

[6] M. Constantin, D. E. Constantin, P. J. Keall, A. Narula, M. Svatos, and J. Perl. Linking computer-aided design (CAD) to Geant4-based Monte Carlo simulations for precise implementation of complex treatment head geometries. *Physics in Medicine and Biology*, 55:–211, 2010.

[7] C.M. Poole, I. Cornelius, J.V. Trapp, and C.M. Langton. A cad interface for geant4. *Accepted, Australasian Physical & Engineering Science in Medicine*, 2012.

[8] N.S. Rehfeld, S. Stute, J. Apostolakis, M. Soret, and I. Buvat. Introducing improved voxel navigation and fictitious interaction tracking in gate for enhanced efficiency. *Physics in medicine and biology*, 54:2163, 2009.

[9] J. Schümann, H. Paganetti, J. Shin, B. Faddegon, and J. Perl. Efficient voxel navigation for proton therapy dose calculation in topas and geant4. *Physics in Medicine and Biology*, 57(11):3281, 2012.

[10] H. Jiang and H. Paganetti. Adaptation of geant4 to monte carlo dose calculations based on ct data. *Medical physics*, 31:2811, 2004.

[11] P. Arce, J. Apostolakis, and G. Cosmo. A technique for optimised navigation in regular geometries. In *Nuclear Science Symposium Conference Record, 2008. NSS'08. IEEE*, pages 857–859. IEEE, 2008.

[12] V. Hubert-Tremblay, L. Archambault, D. Tubic, R. Roy, and L. Beaulieu. Octree indexing of dicom images for voxel number reduction and improvement of monte carlo simulation computing efficiency. *Medical physics*, 33:2819, 2006.

[13] T. Aso, A. Kimura, T. Yamashita, and T. Sasaki. Optimization of patient geometry based on ct data in geant4 for medical application. In *Nuclear Science Symposium Conference Record, 2007. NSS'07. IEEE*, volume 4, pages 2576–2580. IEEE, 2007.

[14] U. Schneider, E. Pedroni, and A. Lomax. The calibration of ct hounsfield units for radiotherapy treatment planning. *Physics in medicine and biology*, 41:111, 1996.

[15] W. Schneider, T. Bortfeld, and W. Schlegel. Correlation between ct numbers and tissue parameters needed for monte carlo simulations of clinical dose distributions. *Physics in medicine and biology*, 45:459, 2000.

[16] S. Guatelli, B. Mascialino, M.G. Pia, and W. Pokorski. Geant4 anthropomorphic phantoms. In *Nuclear Science Symposium Conference Record, 2006. IEEE*, volume 3, pages 1359–1362. IEEE, 2006.

[17] J. Peter, M. P. Tornai, and R. J. Jaszczak. Analytical versus voxelized phantom representation for Monte Carlo simulation in radiological imaging. *Medical Imaging, IEEE Transactions on*, 19(5):556–564, 2002.

[18] D. Sarrut and L. Guigues. Region-oriented CT image representation for reducing computing time of Monte Carlo simulations. *Medical physics*, 35:1452, 2008.

[19] H. Zaidi and X.G. Xu. Computational anthropomorphic models of the human anatomy: the path to realistic monte carlo modeling in radiological sciences. *Annu. Rev. Biomed. Eng.*, 9:471–500, 2007.

[20] J. Zhu, S. Zhao, Y. Ye, and G. Wang. Computed tomography simulation with superquadrics. *Medical physics*, 32:3136, 2005.

[21] Digital Imaging and Communications in Medicine (DICOM). National Electrical Manufacturers Association, 2011.

[22] H. Paganetti, H. Jiang, and A. Trofimov. 4d monte carlo simulation of proton beam scanning: modelling of variations in time and space to study the interplay between scanning pattern and time-dependent patient geometry. *Physics in medicine and biology*, 50:983, 2005.

[23] H. Paganetti, H. Jiang, J. A. Adams, G. T. Chen, and E. Rietzel. Monte Carlo simulations with time-dependent geometries to investigate effects of organ motion with high temporal resolution. *International Journal of Radiation Oncology* Biology* Physics*, 60(3):942–950, 2004.

[24] H. Paganetti. Four-dimensional monte carlo simulation of time-dependent geometries. *Physics in medicine and biology*, 49:N75, 2004.

[25] M. Kazhdan, M. Bolitho, and H. Hoppe. Poisson surface reconstruction. In *Proceedings of the fourth Eurographics symposium on Geometry processing*, pages 61–70. Eurographics Association, 2006.

[26] C.M. Poole, I. Cornelius, J.V. Trapp, and C.M. Langton. Fast tessellated solid navigation in geant4. *Nuclear Science, IEEE Transactions on*, 59(4):1695–1701, 2012.

[27] M. Wendling, L.J. Zijp, L.N. McDermott, E.J. Smit, J.J. Sonke, B.J. Mijnheer, and M. van Herk. A fast algorithm for gamma evaluation in 3d. *Medical physics*, 34:1647, 2007.

[28] D.A. Low and J.F. Dempsey. Evaluation of the gamma dose distribution comparison method. *Medical Physics*, 30:2455, 2003.

[29] IA Popescu, CP Shaw, SF Zavgorodni, and WA Beckham. Absolute dose calculations for monte carlo simulations of radiotherapy beams. *Physics in medicine and biology*, 50:3375, 2005.

Chapter 7

A hybrid radiation detector for simultaneous spatial and temporal dosimetry

Target Journal

Australasian College of Physical Scientists and Engineers in Medicine

Publication Status

Accepted for publication, June 2011.

Authors

CM Poole[1] *(Candidate)*, JV Trapp[1,†], J Kenny[2], T Kairn[2], K Willians[3], M Taylor[3], R Franich[3] and CM Langton[1,⋆]

[1] School of Chemistry, Physics and Mechanical Engineering, Science and Engineering Faculty, Queensland University of Technology
[2] Premion, The Wesley Medical Centre, Brisbane, Australia
[3] School of Applied Sciences, RMIT University, Melbourne, Australia

⋆ Supervisor
† Associate supervisor

Statement of Joint Authorship

JVT conceived the overall concept, wrote the paper, assisted and advised CMP in development and testing of the modified electronics. CMP constructed the scintillation components, built, tested and modified the design of the scintillator electronics, and performed the measurements. JT, CMP and TK designed the experiment. All authors contributed to the experimental design and data collection.

Australas Phys Eng Sci Med
DOI 10.1007/s13246-011-0081-5

SCIENTIFIC PAPER

A hybrid radiation detector for simultaneous spatial and temporal dosimetry

C. Poole · J. V. Trapp · J. Kenny · T. Kairn · K. Williams · M. Taylor · R. Franich · C. M. Langton

Received: 15 February 2011 / Accepted: 1 June 2011
© Australasian College of Physical Scientists and Engineers in Medicine 2011

Abstract In this feasibility study an organic plastic scintillator is calibrated against ionisation chamber measurements and then embedded in a polymer gel dosimeter to obtain a quasi-4D radiation detector. This hybrid dosimeter was irradiated with megavoltage x-rays from a linear accelerator, with temporal measurements of the dose rate being acquired by the scintillator and spatial measurements acquired with the gel dosimeter. The detectors employed in this study are radiologically equivalent; and we show that neither detector perturbs the intensity of the radiation field of the other. By employing these detectors in concert, spatial and temporal variations in the radiation intensity can now be detected and gel dosimeters can be calibrated for absolute dose from a single irradiation.

Keywords Radiotherapy · Dosimetry · Gel dosimetry · Radiation measurement · 4D dosimetry

Introduction

With the increasing clinical use of radiotherapy techniques that rely on the accurate spatial and temporal variation of dose delivery [1–5] there is a growing need for the ability to fully characterise a radiation field, in four dimensions.

Contemporary radiation detectors are capable of measuring radiation dose in one, two, or three dimensions. For example, dosimeters utilizing Fricke solution [6–8], polymers [9–16] and dyed plastics [17, 18] have been successful in measuring radiation dose in three dimensions but not temporally. Electronic portal imaging devices (EPIDs) based on fluoroscopic [19, 20] or solid-state radiation detection [21], as well as planar detector arrays [22] are capable of measuring radiation fields in two spatial dimensions. Recently, diode-array based detectors have been developed which are designed to provide three-dimensional evaluations of delivered dose [23, 24]. All of these dosimeter-array-based systems, including EPIDs, are capable of providing information regarding the variation of the radiation beam with time; however all of these systems (including those specifically designed to measure in three-dimensions) use back-projection techniques, rather than explicit three-dimensional measurement, to provide three-dimensional dosimetric information [23–25].

To date there has been no dosimetry system for measuring radiation dose in three spatial dimensions as well as time. An intermediate solution would be to combine two different radiation detection systems which are radiologically similar, to measure different characteristics of the same radiation field. This technique requires that each detector used must not perturb the measurement of the other. In this feasibility study we combine an organic plastic scintillator for temporal measurements with a polymer gel dosimeter for 3D spatial measurements to produce a quasi four-dimensional hybrid radiation dosimetry system.

C. Poole · J. V. Trapp (✉) · C. M. Langton
Physics, Faculty of Science and Technology, Queensland University of Technology, GPO Box 2434, Brisbane, QLD 4001, Australia
e-mail: j.trapp@qut.edu.au

J. Kenny · T. Kairn
Premion, The Wesley Medical Centre, Suite 1, 40 Chasely Street, Auchenflower, Brisbane, QLD 4066, Australia

K. Williams · M. Taylor · R. Franich
School of Applied Sciences, RMIT University, GPO Box 2476, Melbourne 3001, Australia

Published online: 16 June 2011

Methods and materials

The dosimetry was achieved by combing a BC-428 organic plastic scintillator rod of 5 mm diameter and 6 mm length (Saint Gobain, Paris) for temporal measurements, with a PAGAT polymer gel dosimeter [16] for spatial measurement. The densities of the PAGAT [16] gel dosimeter and organic plastic scintillators are closely matched at 1.026 ± 0.02 [16] and 1.032 g/cm^3 [26], respectively and a previous Monte Carlo study has shown that these two detectors are dosimetrically similar [27]. The scintillator was optically coupled to a S2386-44 K photodiode (Hammamatsu, Japan) and electronic circuitry similar to that described elsewhere [28]. Both the scintillator and the gel dosimeter were encased in an acrylic cylinder container of 13 cm outer diameter and 15 cm length, with walls of 5 mm thickness.

Dose and dose rate responses of the scintillator were calibrated with a 6 MV photon beam produced using a Clinac 6EX (Varian Inc., CA, USA) clinical linear accelerator. The scintillator was positioned on-axis within a Virtual Water (Standard Imaging, WI, USA) phantom at 100 cm SSD, a depth of 4.5 cm and irradiated with a 3×3 cm field. The scintillator was then irradiated at various dose rates as shown in Fig. 2 by varying the monitor units per minute and compared to calibrated ionization chamber data from an A16 Extradin Microchamber.

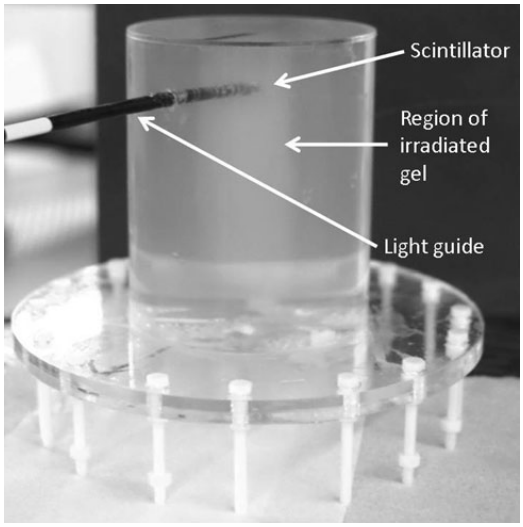

Fig. 1 The scintillator/gel dosimeter immediately after irradiation. Two beams of different intensities were used and neither the container nor linear accelerator were moved between beams, therefore both beams irradiated the system in identical geometry. The optical changes to the gel dosimeter resulting from the radiation dose can be seen along the central axis of the container

The signal was taken as the mean output frequency of the detector electronics [28] sampled at regular intervals and the uncertainty was the standard deviation of the measurements. An angle of 90° between the axis of the beam and the fibre optic coupling was maintained. After calibration, the scintillator was secured in place at the central axis of the cylindrical acrylic container at a location 3 cm from the end wall, and such that the optical coupling fibre penetrated the outer wall of the container at the same height as shown in Fig. 1.

The gel dosimeter was manufactured according to the composition published by Venning et al. [16], however the concentration of Tetrakis hydroxy phosphonium chloride was increased to 8 mM for improved stability [29] as shown at Table 1. Before cooling and setting, the gel dosimeter was poured into the acrylic container containing the scintillator so that the scintillator was completely immersed as shown in Fig. 1. The container was then placed in a refrigerator and stored at 4°C for 24 h to allow the gel dosimeter to set, after which it was pre-scanned in

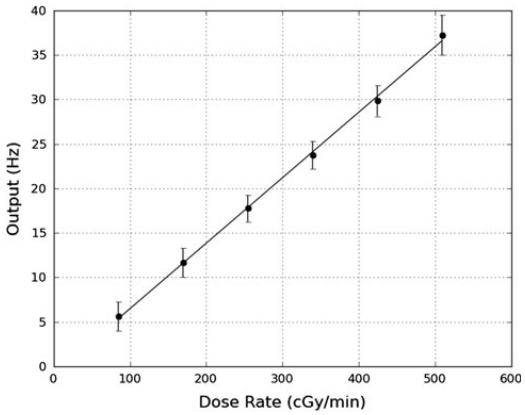

Fig. 2 Data for the calibration of the organic plastic scintillator. The scintillator system outputs a signal whose frequency varies with dose. A linear response is noted for the range of dose rates covered in this study

Table 1 Composition of 1 kg of PAGAT gel dosimeter

Component
Water 859.5 g
Gelatin 300 bloom type A 50 g
N,N′ Methylene bis acrylamide 45 g
Acrylamide 45 g
Hydroquinone 0.001 g
Tetrakis hydroxy phosphonium chloride 1.0 g

an MGS Research IQScan optical CT scanner (MGS Research, Madison, CT, USA).

The container enclosing the scintillator and gel dosimeter was then irradiated with two 3 × 3 cm 6 MV X-ray beams from the same linear accelerator that was used for calibration of the scintillator, with 2 cm of solid water placed on top of the container. This ensured that any effects of Cerenkov radiation equally applied to both the calibration and the irradiation. Both radiation beams were delivered to the same location and orientation (centrally along the cylindrical axis); however the radiation output of the linear accelerator was varied so that they produced 2.50 ± 0.03 Gy/minute for 60 s and 5.00 ± 0.05 Gy/minute for 30 s at the scintillator, respectively, giving a total dose of 5 Gy. Because the scintillator and sheath were directly in contact with the gel dosimeter, electronic equilibrium was not disturbed at the boundary as shown previously [27]. The dose rates of the beams were measured with the scintillator at the time of delivery. It has been shown [30, 31] that dose rate effects within PAGAT gel dosimeters are negligible for the range of dose rates and total dose delivered in this experiment.

After 24 h the container enclosing the gel dosimeter and the scintillator was scanned in a MGS Research IQScan optical CT scanner (Madison, CT, USA). The pre-scan data was then subtracted prior to image reconstruction to remove optical inhomogeneities in the gel. Data processing was performed using Matlab (The Mathworks, USA).

Results

Figure 2 shows the calibration data for the scintillator and shows an increasing response of output with respect to increasing dose rate. The data provides an R^2 value of 0.998 and P value of 6×10^{-7} for a 95% confidence level. From this data we make the assumption of a linear dose rate response of the total scintillator measurement for those dose rates employed in this study. Possible contributions from Cerenkov radiation to the signal are discussed in the following section.

Figure 3 qualitatively demonstrates the spatial distribution provided by the gel dosimeter, showing an isosurface representation of the reconstructed optical CT image, with contours selected at 64 and 83% of d_{max}. When using this technique to analyse a radiation field one would select contours at whichever level is required for purpose. Acquisition of optical CT data in slices occupied by the scintillator is corrupted as the scintillator and masking sheath is optically opaque and thus leads to artefacts arising from the undersampling of projections through these slices. Therefore slices corresponding to the scintillator and those immediately surrounding have been removed from Fig. 3.

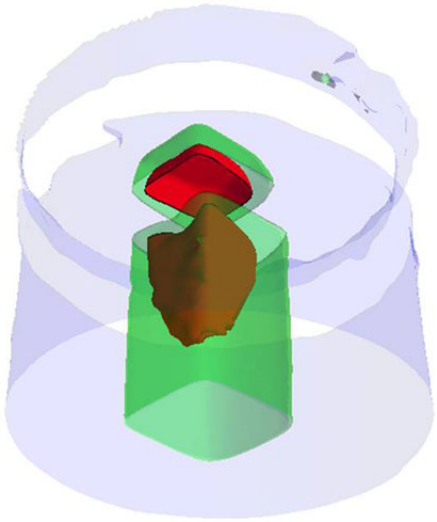

Fig. 3 Typical 3D isosurfaces acquired from the post irradiation optical CT image of the gel dosimeter as located in the container (*blue*). Because the optical density is proportional to radiation dose, the isosurface can be converted to a dose contour. In this case the *green surface* represents 64% of the maximum dose and the (*darker*) *red* represents 83% of the maximum dose

The data loss is an artefact only and in practical use the scintillator is recommended to be placed away from key locations in the radiation field to ensure no loss of critical spatial data.

Figure 4 shows the temporal radiation dose measurement at the location of the scintillator. The temporal scintillator data clearly shows the presence of two beams at different times, intensities, and duration. Because the

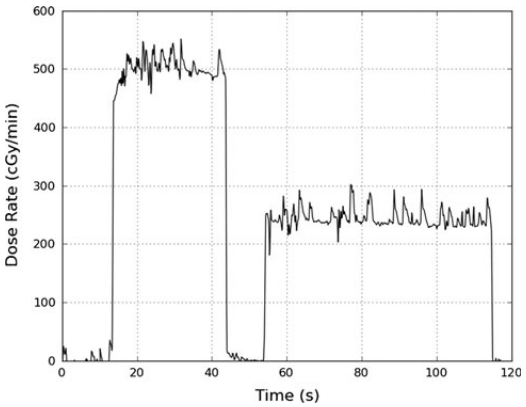

Fig. 4 Temporal organic plastic scintillator measurement during the irradiation of the container. Although the same dose was delivered with each beam, the dose rate and time was varied

scintillator has been pre-calibrated, the measured data will also indicate any errors in the output of the linear accelerator, both in radiation dose rate or exposure time. This would not otherwise be apparent in a 3D gel dosimeter measurement alone. Noise in the figure is due to quantum noise in the detector electronics as well as contributions from beam fluctuations at the time of sampling.

Ideally, the measurements of each detector should not be perturbed by the presence of the other. For example, if the scintillator was of a significantly different density, the radiation dose received by the gel dosimeter would show a 'shadow' of the scintillator in critical 'downstream' regions. Figure 5 shows comparative plots of the optical density of the gel dosimeter along the direction of the radiation beam, with error bars representing the standard deviation of the surrounding 3×3 mm region. Represented in the figure are depth dose data along the central axis of the beam which passes through the centre of the scintillator, and off axis data located within the radiation field in the gel dosimeter but not passing through the scintillator. The figure clearly shows the expected depth-dose curve as the beam transits the gel dosimeter in both sets of data located within the radiation field with a loss of data in the slices corresponding to the location of the scintillator. There is a region of reduced gel response immediately surrounding the location of the scintillator. Oxygen contamination decreases the sensitivity of polymer gel dosimeters [14] and it is likely that the presence of the scintillator and sheath in the gel allowed diffusion of oxygen in the time between manufacture, irradiation and imaging, thus suppressing the response of the gel to radiation. Previous studies with acrylamide based gels have shown that oxygen diffuses at a rate of 8 $(\pm 2) \times 10^{-6}$ cm^1 s^{-1} [32]. At regions of further depth the depth dose data for both in-field measurements match, thus showing negligible perturbation of dose further downstream by the scintillator. Therefore, these results suggest that this technique would be suitable for use providing the scintillator is placed further than 1 cm from critical regions in the irradiation.

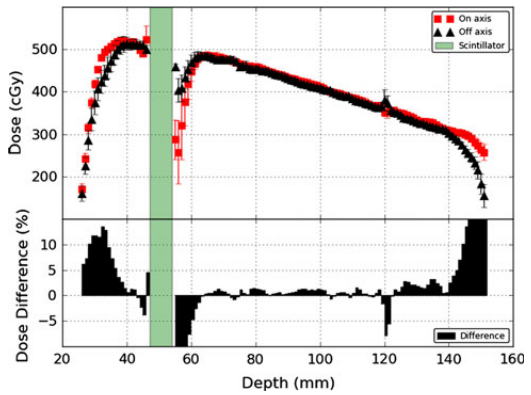

Fig. 5 Changes in the gel dosimeter optical density along the axis of the cylinder. The *upper panel* shows the optical CT data for two sets of in-field data: one intersecting the scintillator and the other within the radiation field but not intersecting the scintillator. The *bottom panel* shows the difference between the two data sets

Discussion

The interpretation of the data from these measurements will naturally depend on the response characteristics of each of the detectors; good practice would therefore necessitate each detector to be fully characterised before use. For example, the PAGAT type gel dosimeter used here for the 3D spatial dose mapping has previously been shown to have an asymptotic relationship to total dose [16]; conversions of optical density data, shown in Fig. 3, to dose must therefore account for this relationship. It should be noted however that in PAGAT gel dosimeters a linear relationship between optical density and dose is generally assumed up to 7 Gy [16]; the maximum dose used here was less than this amount and therefore a linear dose response has been approximated in this study.

In addition to providing quasi-4D dosimetry, this method enhances traditional gel dosimetry measurements by enabling a calibrated dose point to be acquired within the gel itself. Previously gel dosimeters have been restricted to either relative dose measurements or calibration via secondary methods such as separate vials or reproduction of an identical gel in a second container, both methods of which may affect the response of the gel dosimeter through variations in chemical composition, temperature history [33–35] or dose inaccuracies resulting from varying scatter conditions in different container geometries [36, 37]. Furthermore, Taylor et al. [36, 37] have shown that a single large container is the most dosimetrically accurate geometry for gel dosimetry; inclusion of both detectors in the same volume ensures the most accurate results. Therefore, the inclusion of a plastic scintillator in a large container provides the opportunity for absolute dose measurements with gel dosimetry. Future study is required to refine the technique used in this feasibility study, for example the reduction of oxygen contamination at the immediate surrounds of the scintillator requires attention.

The extraction of the dose information is not restricted to optical computed tomography, for example, it has been shown that there is minimal interference with MRI image quality with the presence of a scintillating fibre within a gel dosimeter [38, 39]. The detectors that can be used in this technique are not restricted to those employed here, for

example, an excellent candidate for the 3D spatial detector would be polyurethane PRESAGE dosimeters [17] which would alleviate the requirement to remove data close to the scintillator and walls due to oxygen contamination. Similarly, for the nuclear industry and other industrial uses, detectors such as the RadBall [40, 41] could provide a suitable spatial detector, or in the case of very high dose rate materials such as plastics [42] have been shown to react to ionising radiation and would combine well with the temporal measurements of an organic plastic scintillator.

The existence of Cerenkov radiation in the scintillator and optical fibre will cause an additional component to the signal. Several authors have discussed approaches to reduce interference of Cerenkov radiation in plastic scintillator measurements [43–46]. In our case the effects of Cerenkov radiation within the scintillator and optical fibre was minimized due to a 90° irradiation angle and selection of components spectrally incompatible with Cerenkov light; however it is likely that the measured signal does contain a component of Cerenkov radiation. Because the same volume of optical coupling fibre (and full volume of the scintillator) was irradiated in both the calibration and the container irradiation, the same proportion of Cerenkov radiation occurred on both occasions and thus the calibration is adequate for this equivalent geometry and beam energy. Therefore, for the technique described in this study to be reliable it requires that the same volume of scintillator and optical fibre be irradiated at calibration and use. For applications where a different amount of the optical coupling fibre is irradiated by each beam (for example IMRT), an alternative Cerenkov rejection approach should be used [46–48].

Conclusion

In this study we have shown that the combination of two radiation detectors, one providing a 3D spatial mapping of dose and one providing temporal variation in dose rate, can be used to produce a quasi 4D-hybrid radiation detection system. Typically, a gel dosimeter only provides dose information integrated over time, thus temporal information is lost. This study shows that the novel addition of temporal information to integrating 3D spatial dosimetry has been demonstrated to be feasible. This technique will provide a valuable means to fully characterize ionizing radiation fields.

Acknowledgments This work was partly funded by the Queensland Cancer Physics Collaborative and Cancer Australia (Department of Health and Ageing) Research Grant 614217. We would like to thank Greg Pedrazzini from Premion for assistance in calibration of the scintillator.

References

1. Schulz RJ, Kagan AR (2002) On the role of intensity-modulated radiation therapy in radiation oncology. Med Phys 29(7): 1473–1482
2. Descovich M, Fowble B, Bevan A, Shchechter N, Park C, Xia P (2010) Comparison between hybrid direct aperture optimized intensity modulated radiotherapy and forward planning intensity modulated radiotherapy for whole breast irradiation. Int J Radiat Oncol Biol Phys 76:91–99
3. Evans PM, Donovan EM, Partridge M, Childs PJ, Convery DN, Suter BL, Yarnold JR (2000) The delivery of intensity modulated radiotherapy to breast using multiple static fields. Radiother Oncol 57:79–89
4. Bortfield T (2006) IMRT: a review and preview. Phys Med Biol 51:R363–R379
5. Dieterich S, Cleary K, D'Souza W, Murphy M, Wonh KH, Keall P (2008) Locating and targeting moving tumors with radiation beams. Med Phys 35(12):5684–5694
6. Fricke H, Morse S (1927) The chemical action of roentgen rays on dilute ferrous sulfate solutions as a measure of radiation dose. Am J Roentgenol Radium Ther Nucl Med 18:430–432
7. Gore JC, Kang YS, Schulz RJ (1984) Measurement of radiation dose distributions by nuclear magnetic resonance (NMR) imaging. Phys Med Biol 29:1189–1197
8. Gore JC, Kang YS, Schulz RJ (1990) Dose-response curves for Fricke-infused agarose gels as obtained by nuclear magnetic resonance. Phys Med Biol 34:1611–1622
9. Baldock C, De Deene Y, Doran SJ, Ibbott GS, Jirasek A, Lepage M, McAuley KB, Oldham M, Schreiner LJ (2010) Polymer gel dosimetry. Phys Med Biol 55(5):R1–63
10. Day MJ, Stein G (1950) Chemical effects of ionizing radiation in some gels. Nature 166:1146–1147
11. Mesrobian RB, Ander P, Ballantine DS, Dienes GJ (1954) Gamma-ray polymerization of acrylamide in the solid state. J Chem Phys 22:565–566
12. Andrews HL, Murphy RE, LeBrun EJ (1957) Gel dosimeter for depth dose measurements. Rev Sci Instrum 28:329–332
13. Maryanski MJ, Gore JC, Kennan RP, Schulz RJ (1993) NMR relaxation enhancement in gels polymerized and cross-linked by ionizing radiation: a new approach to 3D dosimetry by MRI. Magn Reson Imaging 11:253–258
14. Maryanski MJ, Schulz RJ, Ibbott GS, Gatenby JC, Xie J, Horton D, Gore JC (1994) Magnetic resonance imaging of radiation dose distributions using a polymer-gel dosimeter. Phys Med Biol 39:1437–1455
15. Fong PM, Keil DC, Does MD, Gore JC (2001) Polymer gels for magnetic resonance imaging of radiation dose distributions at normal room atmosphere. Phys Med Biol 46:3105–3113
16. Venning A, Hill B, Brindha S, Healy BJ, Baldock C (2005) Investigation of PAGAT polymer gel dosimeter using magnetic resonance imaging. Phys Med Biol 50:3875–3888
17. Adamovics JA, Maryanski MJ (2006) Characterisation of PRESAGE (TM): a new 3-D radiochromic solid polymer dosemeter for ionising radiation. Radiat Prot Dosim 120:107–112
18. Gorjiara T, Hill R, Kuncic Z, Adamovics JA, Bosi S, Kim J, Baldock C (2011) Investigation of radiological properties and water equivalency of PRESAGE® dosimeters. Med Phys 38(4):2265–2274
19. Baily NA, Horn RA, Kampp TD (1980) Flouroscopic visualization of megavoltage therapeutic X-ray beams. Int J Radiat Oncol Biol Phys 6:935–939
20. Meertens H, van Herk M, Weeds J (1984) A liquid ionization detector for digital radiography of therapeutic megavoltage photon beams. Phys Med Biol 30:313–321

21. van Etmpt W, McDermott L, Nijsten S, Wendling M, Lambin P, Mijnheer B (2008) A literature review of electronic portal imaging for radiotherapy dosimetry. Radiother Oncol 88(3): 289–309
22. Jursinic PA, Nelms BE (2003) A 2-D diode array and analysis software for verification of intensity modulated radiation therapy delivery. Med Phys 30(5):870–879
23. Feygelman V, Opp D, Javedan K, Saini AJ, Zhang G (2010) Evaluation of a 3D diode array dosimeter for helical tomotherapy delivery QA. Med Dosim 35(4):324–329
24. Yan GH, Lu B, Kozelka J, Liu C, Li JG (2010) Calibration of a novel four-dimensional diode array. Med Phys 37(1):108–115
25. van Elmpt W, McDermott L, Nijsten S, Wendling M, Lambin P, Mijnheer B (2008) A literature review of electronic portal imaging for radiotherapy dosimetry. Radiother Oncol 88(3): 289–309
26. Saint Gobain (2008) Scintillation products. Saint Gobain Ceramics & Plastics, Louisville
27. Trapp JV, Kairn T, Crowe S, Fielding A (2009) Internal calibration of gel dosimeters: a feasibility study. J Phys 164 (012014):1–5
28. Williams K, Robinson N, Trapp JV, Ackerly T, Das R, Kemp P, Geso M (2007) A portable organic plastic scintillator dosimetry system for low energy X-rays: a feasibility study using an intraoperative X-ray unit as the radiation source. J Med Phys 32(2):73–76
29. Khoei S, Moorrees JB, Langton CM, Trapp J (2010) An investigation of the pre-irradiation temporal stability of PAGAT gel dosimeters. J Phys 250:012019
30. De Deene Y, Vergote K, Claeys C, De Wagter C (2006) The fundamental radiation properties of normoxic polymer gel dosimeters: a comparison between a methacrylic acid based gel and acrylamide based gels. Phys Med Biol 51:653–673
31. Karlsson A, Gustavsson H, Mansson S, McAuley KB, Back SAJ (2007) Dose integration characteristics in normoxic polymer gel dosimetry investigated using sequential beam irradiation. Phys Med Biol 52:4697–4706
32. Hepworth S, Leach MO, Doran SJ (1999) Dynamics of polymerization in polyacrylamide gel (PAG) dosimeters: (II) modelling oxygen diffusion. Phys Med Biol 44:1875–1884
33. De Deene Y, Hanselaer P, De Wagter C, Achten E, De Neve W (2000) An investigation of the chemical stability of a monomer/polymer gel dosimeter. Phys Med Biol 45:859–878
34. Dumas E, Leclerc G, Lepage M (2006) Effect of container size on the accuracy of polymer gel dosimetry. J Phys 56:239–241
35. De Deene Y, Pittomvils G, Visalatchi S (2007) The influence of cooling rate on the accuracy of normoxic polymer gel dosimeters. Phys Med Biol 52:2719–2728
36. Taylor ML, Franich R, Johnston PN, Miller M, Trapp JV (2007) Systematic variations in polymer gel dosimeter calibration due to container influence and deviations from water equivalence. Phys Med Biol 52:3991–4005
37. Taylor ML, Franich R, Trapp JV, Johnston PN (2009) A comparative study of the effect of calibration conditions on the water equivalence of a range of gel dosimeters. IEEE Trans Nucl Sci 56(2):429–436
38. Archambault L, Leclerc G, Beaulieu L, Lepage M (2006) Absolute calibration of polymer gel dosimeter using scintillating fibres. J Phys 56:242–244
39. Tremblay NM, Hubert-Tremblay V, Bujold R, Beaulieu L, Lepage M (2010) Improvement in the accuracy of polymer gel dosimeters using scintillating fibres. J Phys 250:10.1088
40. Doran SJ, Stanley SJ, Jenneson PM, Prott E, Adamovics JA (2009) RadBall: a new departure for 3D dosimetry. J Phys 164:012042
41. Farfan EB, Foley TQ, Jannik GT, Harpring LJ, Gordon JR, Blessing R, Coleman JR, Holmes CJ, Oldham M, Adamovics JA, Stanley SJ (2010) RadBall technology testing in the Savannah River site's Health Physics Instrument Calibration Laboratory. J Phys 250(1):398–402. doi:10.1088/1742-6596/250/1/012080
42. Boag JW, Dolphin GW, Rotblat J (1958) Radiation dosimetry by transparent plastics. Radiat Res 9:589–610
43. Beddar AS, Mackie TR, Attix FH (1992) Water-equivalent plastic scintillation detectors for high-energy beam dosimetry: I physical characteristics and theoretical considerations. Phys Med Biol 37(10):1883–1900
44. deBoer SF, Beddar AS, Rawlinson JA (1993) Optical filtering and spectral measurements of radiation induced light in plastic scintillation dosimetry. Phys Med Biol 38:945–958
45. Fontbonne JM, Iltis G, Ban G, Battala A, Vernhes JC, Tillier J, Bellaize N, Tamain B, Mercier K, Motin JC (2002) Scintillating fibre dosimeter for radiation therapy accelerator. IEEE Trans Nucl Sci 49:2223–2227
46. Lambert J, Yin Y, McKenzie DR, Law S, Suchowerska N (2008) Cerenkov-free scintillation dosimetry in external beam radiotherapy with an air core light guide. Phys Med Biol 53:3071–3080
47. Archambault L, Briere TM, Ponisch F, Beaulieu L, Kuban DA, Lee A, Beddar S (2010) Toward a real-time in vivo dosimetry system using plastic scintillation detectors. Int J Radiat Oncol Biol Phys 78(1):280–287
48. Beddar AS, Law S, Suchowerska N, Mackie TR (2003) Plastic scintillation dosimetry: optimization of light collection efficiency. Phys Med Biol 48:1141–1152

Chapter 8

Conclusions & Future Directions

Significant computing resources are always required when performing Monte Carlo simulations for the purposes of radiotherapy dose calculation. Generally the computational requirement is so significant it renders the benefits of using the Monte Carlo method in the first place too expensive – defaulting to faster analytical methods that produce adequate results without massive computational costs is an easier option. This work has shown that the magnitude of this requirement can be reduced by alternative geometry definitions and the use of cloud computing for performing Monte Carlo simulations.

8.1 Summary of Outcomes

True supercomputing infrastructure is usually reserved for universities and government institutions due to the high cost of maintenance and consumables, such as cooling and electricity. With the advent of cloud computing however, vast (100's of machines) compute resources can be acquired quickly and easily though a web browser on a standard desktop computer or laptop. Chapter 3 demonstrates the effectiveness of cloud computing when applied to radiotherapy dose calculation.

This work makes available such a great deal of computing resources to the

average user, even highly time consuming computations may be performed in a relatively short period of time assuming the problem may be split up into small jobs that can be executed simultaneously; as is the case for radiotherapy dose calculations using Monte Carlo. The test cases used to demonstrate this technology were generally of a type that do not require large network transfers of data; this technology may not be suitable for problems that require very large data transfers, however radiotherapy dose calculation does not impose this limitation, thereby making it ideal to exploit the cloud computing platform. Cost blow-out may also occur on poorly managed accounts where compute instances are left on when not being used. Further work will expand the software tools described in chapter 3 to enable does calculations using other Monte Carlo toolkits.

Definition of the experimental geometry, whether it be a patient geometry definition or otherwise is key to the accuracy of a simulation, especially when considering radiotherapy dose calculation using Monte Carlo. Following this, it is of great importance that the simulation geometry is an adequate reproduction of the experiment geometry; considering the definition of a clinical linear accelerator treatment head, more complex components such as the flattening filter can not easily be described by a single primitive such as a cube or sphere. Tessellated meshes such as those created using computer aided design software packages offer the most direct coupling between component design and manufacture and the simulation geometry. Accordingly, the technique for direct CAD geometry import into GEANT4 described in chapter 4 demonstrates the effectiveness of this concept. This CAD interface can be used for any Monte Carlo simulation that has complex components that are more easily created using CAD software, not just simulations limited to calculations for medical physics applications.

Presently the CAD interface is limited to five file formates as described in chapter 4, as development continues more file formats are being added to the `cadmesh` library. Further to this, the CAD interface requires VCGLIB as an external software dependency - whilst this does provide some complication to

the installation and compilation process over a standalone library, the additional functionality provided by VCGLIB, including various mesh manipulation routines, is highly useful in the simulation environment when the manipulation of such geometries is required. Indeed the usefulness of this tool has already been embraced by the wider GEANT4 community with over 100 downloads of the software since if became available for public use.

High fidelity geometry definitions like those derived from CAD however, arrest the performance of a given Monte Carlo simulation; this is most certainly the case for tessellated surfaces geometries in GEANT4. In chapter 5 we examine the root cause of this effect. Principally, the requirement to consider the entire solid, one which may be defined by a collection of many facets, when determining the current location within the solid is what cases the arrest in navigation performance. Geometry optimisation techniques already present within the GEANT4 toolkit such as volume parameterisation and smart voxelisation are only applicable to geometries that are constructed from many smaller constituent parts. By exploiting these optimisation techniques already present within the toolkit we show that a tessellated solid, and indeed nested tessellated solids may be redefined as a collection of individual tetrahedra making up a tetrahedral mesh.

The technique described in chapter 5 has been included as functionality in the aforementioned GEANT4 CAD interface. Currently the process is entirely automatic and transparent to the user given a tessellated mesh described in a supported CAD file format. Whilst being limited however to the tetrahedralisation of triangular tessellated meshes only, this limitation is strictly due to implementation; in principal there is no limiting factor preventing the technique being extended to the tetrahedralisation of quadrangular meshes. Indeed the technique could be applied to arbitrary geometry definitions within GEANT4 made up of collections of other primitive solids. Presently the focus of the development of this technique is to provide automatic and transparent meshing and parameterisation of arbitrary user geometries. Such a development enabling au-

tomatic tetrahedral and parameterisation could provided significant performance increases to pre-existing simulations geometries by making smart voxelisation and other automatic optimisation techniques more readily available. This technique is described and tested with a GEANT4 specific implementation, in principal other Monte Carlo software packages may benefit from the redefinition of complex geometries subdivided by smaller primitive volumes, however this would be subject to the specific geometry navigation implementation.

As with user defined geometries, equivalence between the true patient geometry and the simulation geometry is of great importance and can benefit from the previously mentioned methods. In chapter 6 we offer an alternative patient geometry that uses regions of interest already present within a DICOM-RT radiotherapy treatment plan. Recovering these regions of interest and creating surface meshes from them, which are subsequently loaded using the GEANT4 CAD interface described in chapter 4, provides for a highly flexible patient geometry within the simulation environment. The dosemetric equivalence of this region of interest based geometry was evaluated against the equivalent and source CT dataset. We show that a simple mesh describing only the patients outline or body is sufficient to calculate an equivalent dose distribution had the full CT dataset been used and in less than one twentieth of the time. The implications of this is that a meaningful calculated dose distribution can be acquired very quickly and with presumably less total compute cost.

Whilst there may be situations where the technique is not suitable, at the very least, the speed at which the calculation is performed makes it highly useful for the purposes of simulation debugging and preliminary dosemetric investigation – additionally, the technique allows for the direct visualisation of the patient anatomy relative to the simulated linear accelerator treatment head. When using regions of interest defined in a DICOM-RT treatment plan, the alternative geometry accuracy is highly dependant on the quality of the regions of interest and the methods that were used to segment them from the rest of the CT dataset.

Further work will quantify the effects of variability in the definition of patient geometry subject to the fidelity of the source CT dataset and the regions of interest that are derived from it.

Finally, three-dimensional dose distribution measurements made with a polymer gel dosimeter were difficult to calibrate for absolute dose and did not preserve temporal dose rate information; indeed the dose rate history could not be recovered from an irradiated gel itself. With the combination of a polymer gel dosimeter and a gel or water equivalent organic plastic scintillator dose rate meter, this otherwise lost temporal dose rate information can be preserved without significant perturbation to the three dimensional dose distribution recorded in the gel. Additionally, an organic plastic scintillator calibrated for absolute dose can serve as a calibration point for the gel dosimeter, yielding 3D dose distribution measurements to be recovered from the gel. Whilst every effort was made to avoid perturbation to the dose distribution within in the gel dosimeter as a consequence of the presence of the organic plastic scintillator dosimeter, some perturbation is present; future work will focus on minimising this effect with the use of smaller diameter scintillating components.